Journal of
Medicinal
Chemistry

Discovery of Novel Small-Molecule Antiangiogenesis Agents to Treat Diabetic Retinopathy

Donghwa Kim, Sang Won Choi, Jihee Cho, Jae-Hui Been, Kyoungsun Choi, Wenzhe Jiang, Jaeho Han, Jedo Oh, Changmin Park, Soongyu Choi, Songyi Seo, Koung Li Kim, Wonhee Suh, Sang Kook Lee,* and Sanghee Kim*

Cite This: *J. Med. Chem.* 2021, 64, 5535−5550 Read Online

ACCESS | Metrics & More | Article Recommendations | Supporting Information

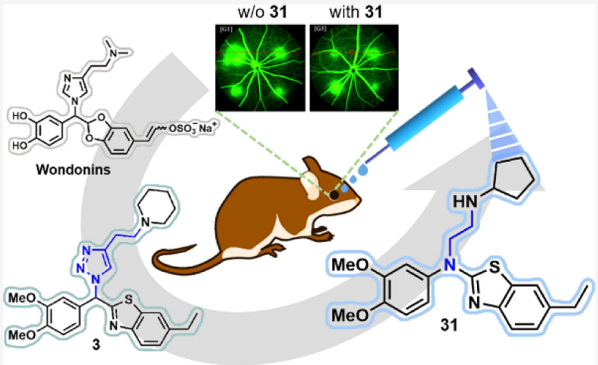

ABSTRACT: Diabetic retinopathy is the leading cause of blindness which is associated with excessive angiogenesis. Using the structure of wondonin marine natural products, we previously created a scaffold to develop a novel type of antiangiogenesis agent that possesses minimized cytotoxicity. To overcome its poor pharmaceutical properties, we further modified the structure. A new scaffold was derived in which the stereogenic carbon was changed to nitrogen and the 1,2,3-triazole ring was replaced by an alkyl chain. By comparing the bioactivity versus cytotoxicity, compound **31** was selected, which has improved aqueous solubility and an enhanced selectivity index. Mechanistically, **31** suppressed angiopoietin-2 (ANGPT2) expression induced by high glucose in retinal cells and exhibited *in vivo* antiangiogenic activity in choroidal neovascularization and oxygen-induced retinopathy mouse models. These results suggest the potential of **31** as a lead to develop antiangiogenic small-molecule drugs to treat diabetic retinopathy and as a chemical tool to elucidate new mechanisms of angiogenesis.

INTRODUCTION

Angiogenesis is the formation of new blood vessels from existing blood vessels, and it plays an important role in embryonic development, wound healing, and the reproductive cycles of women.[1,2] However, uncontrolled angiogenesis increases the risk of various diseases, such as cancer, retinopathy, myocardial infarction, and cerebral infarction.[3] Angiogenesis is finely regulated by various factors such as vascular endothelial growth factor (VEGF), angiopoietin (ANGPT), matrix metalloproteinases (MMPs), platelet-derived growth factor (PDGF), tissue inhibitors of metalloproteinases (TIMPs), interferon-alpha/beta/gamma, plasminogen activators, and cyclooxygenase-2 (COX-2).[3,4] Patient data also suggest that the expression of angiopoietin-2 (ANGPT2) is higher in eyes with retinal detachment than eyes with completely attached retina, and the levels of ANGPT2 are associated with upregulated expressions of matrix metalloproteinase-9 (MMP-9), VEGF, and transforming growth factor beta 1 (TGFβ1).[5]

Diabetic retinopathy is a microvascular complication of diabetes and a leading cause of blindness.[6] High blood sugar levels in diabetic patients can damage blood vessels causing them to swell, leak, and grow quickly, which contributes to the excessive neovascularization and progression of diabetic retinopathy.[7] Almost all patients with type 1 diabetes and more than 60% of patients with type 2 diabetes develop retinopathy over time.[8] Diabetic retinopathy is often treated with surgery, laser therapy, and intravitreous injections of steroids or anti-VEGF biologic drugs such as ranibizumab, bevacizumab, and aflibercept.[9] Anti-VEGFs decrease the severity of the disease and vision, but multiple adverse effects are reported, such as infections from intravitreal injections, inflammation, retinal detachment, and cerebrovascular disease.[10] Therefore, the findings of antiangiogenic small molecules might help overcome the drawbacks of biologic drugs. Currently, no U.S. Food and Drug Administration (FDA)-approved small-molecule drugs are available to treat diabetic retinopathy.

Wondonins (**1** and **2**, Figure 1) are marine natural products possessing novel antiangiogenic properties without overt cytotoxicity. We conceived that these biological properties may have a benefit to develop novel antiangiogenic agents with reduced side effects. In our previous work, we modified the

Received: November 13, 2020
Published: April 27, 2021

https://doi.org/10.1021/acs.jmedchem.0c01965

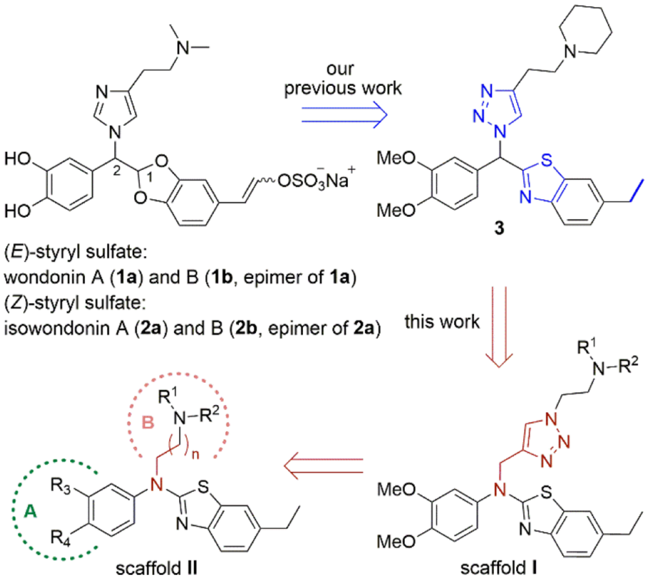

Figure 1. Chemical structures of wondonins and schematic representation of the structural design of the new wondonin analogues.

structure of wondonins using a medicinal chemical rationale to overcome their physicochemical drawbacks.[11] Our efforts led to the discovery of compound **3** with more potent antiangiogenic activity and without overt cytotoxicity to human umbilical vein endothelial cells (HUVECs). Compound **3** is more stable and easily synthesized than the parent natural-product wondonins. However, compound **3** still has a chiral center in its structure, yielding enantiomers. We attempted to obtain **3** in the enantiomerically pure form to investigate the pharmacological difference between the two enantiomers. The enantioselective synthesis of two enantiomers of **3** was not easily accessible by conventional methods. Additionally, the chiral center is prone to epimerization, presumably because it is located adjacent to three aromatic rings.

In the present study, we further modified the structure of wondonins and compound **3** to create more drug-like scaffolds without an epimerizable chiral center. Our efforts resulted in the discovery of new drug-like small compounds that exhibited similar antiangiogenic activity to **3** and sunitinib without notable cytotoxicity. This new type of compound has reduced scaffold complexity and is easily accessible in short synthetic pathways. The molecular mechanisms were also investigated in HUVECs and ocular cells, such as human retinal microvascular endothelial cells (HRMECs) and adult retinal pigment epithelial cell line-19 (ARPE-19) cells, and the *in vivo* efficacy was examined in oxygen-induced retinopathy (OIR) and choroidal neovascularization (CNV) mouse models. Herein, we present our work on a successful scaffold jump of wondonins.

RESULTS AND DISCUSSION

Design and SAR Study. The biological properties of the synthetic wondonin derivatives were assessed by measuring their effects on VEGF-induced tube formation and cytotoxicity in HUVECs. In our previous study, each image of tube formation was quantified by counting the number of branches. To obtain more accurate data, we modified the method to calculate the total segment lengths per image, as described in the Experimental Section. We aimed to identify noncytotoxic antiangiogenic compounds. Therefore, each compound was compared using the selectivity index, which is the ratio of the IC_{50} for tube formation to the IC_{50} for cytotoxicity in HUVECs (Tables 1−4 and Figures S1−S4).

Table 1. VEGF-Induced Tube Formation and Cell Viability in HUVECs According to Amino Group Modifications of Scaffold I (4−7)

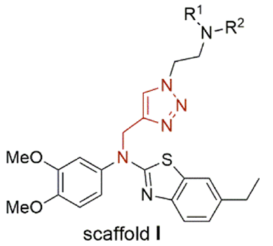

Compd	NR^1R^2	IC_{50} (μM)[a] Tube formation	IC_{50} (μM)[a] Cell viability	SI[b]
3[c]	—	2.77	62.12	22.4
4	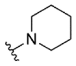	8.22	14.85	1.8
5	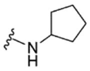	4.73	49.19	10.4
6	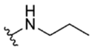	6.15	30.46	5.0
7	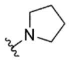	2.36	44.91	19.0

[a] The IC_{50} data are expressed as the means of duplicate experiments. [b] Selectivity index was calculated as the ratio of the IC_{50} values of cell viability and tube formation. [c] The structure of **3** is shown in Figure 1.

As an initial and major structural modification of **3** (Figure 1), the stereogenic carbon atom was replaced by a nitrogen atom. The 1,2,3-triazole and aliphatic amine moieties were maintained, although their bond connectivity was altered. Such

Table 2. VEGF-Induced Tube Formation and Cell Viability of Scaffold II-A (8−11)

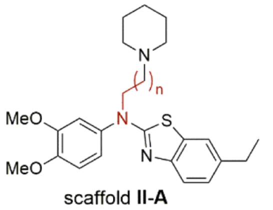

Compd	IC_{50} (μM)[a] tube formation	IC_{50} (μM)[a] cell viability	SI[b]
8, *n* = 1	9.04	>100	11.1
9, *n* = 2	2.31	49.95	21.6
10, *n* = 3	3.28	55.06	16.8
11, *n* = 4	3.47	38.19	11.0

[a] The IC_{50} data are expressed as the means of duplicate experiments. [b] Selectivity index was calculated as the ratio of the IC_{50} values of cell viability and tube formation.

Table 3. VEGF-Induced Tube Formation and Cell Viability in HUVECs According to the Phenyl Moiety Modification of the Piperidine-Introduced Scaffold II (12−14)

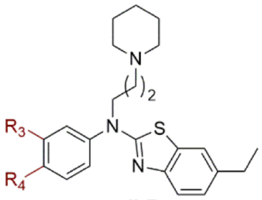

scaffold **II-B**

	A moiety		IC_{50} (μM)[a]		
compd	R^3	R^4	tube formation	cell viability	SI[b]
12	OCH_3	H	5.17	17.34	3.4
13	F	F	1.98	10.60	5.4
14	H	CH_3	0.92	8.50	9.2

[a]The IC_{50} data are expressed as the mean of duplicate experiments. [b]Selectivity index was calculated as the ratio of the IC_{50} values of cell viability and tube formation.

Table 4. VEGF-Induced Tube Formation and Cell Viability in HUVECs According to Changes in the Amino Group and Alkylchain Length of Scaffold II (15−34)

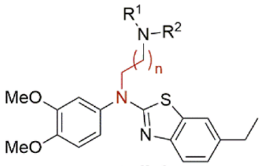

scaffold **II-C**

Compd	B moiety	IC_{50} (μM)[a]		SI[b]
	NR^1R^2	Tube formation	Cell viability	
15, n = 1	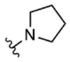	6.33	94.83	15.0
16, n = 2		14.93	> 100	6.7
17, n = 3		20.43	48.81	2.4
18, n = 4		15.84	9.89	0.6
19, n = 1	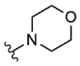	5.36	> 100	18.7
20, n = 2		9.04	> 100	11.1
21, n = 3		29.86	> 100	3.3
22, n = 4		10.32	69.34	6.7
23, n = 1	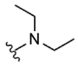	13.90	> 100	7.2
24, n = 2		15.66	> 100	6.4
25, n = 3		24.67	> 100	4.1
26, n = 4		24.51	> 100	4.1
27, n = 1	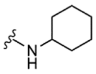	17.69	> 100	5.7
28, n = 2		19.64	41.95	2.1
29, n = 3		1.82	19.45	10.7
30, n = 4		6.51	11.06	1.7
31, n = 1	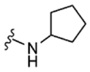	2.95	> 100	33.9
32, n = 2		23.83	98.68	4.1
33, n = 3		2.34	31.66	13.5
34, n = 4		10.19	7.55	0.7

[a]The IC_{50} data are expressed as the means of duplicate experiments. [b]Selectivity index was calculated as the ratio of the IC_{50} values of cell viability and tube formation.

structural modification resulted in scaffold **I**. The first compound with this scaffold was **4** (Table 1) with a piperidine ring, showing notable inhibitory activity against tube formation in VEGF-induced HUVECs. However, **4** exhibited a lower selectivity index than its parent compound **3**.

Because we previously showed that the inhibitory effects on both tube formation and cytotoxicity were sensitive to amino group modifications, several amino groups other than piperidine were screened to further evaluate the possibility of using **I** as a new scaffold of novel antiangiogenesis agents. Compound **5** with a cyclopentylamino group showed an approximately twofold increase in tube formation inhibition and a threefold decrease in cytotoxicity compared with **4**. The propyl amine analogue **6** displayed a similar activity profile to **4**. Notably, compound **7**, with a pyrrolidine moiety, was three times more potent than the piperidine analogue **4** and three times less cytotoxic against HUVECs, exhibiting a selectivity index of 19 similar to that of **3**. These results indicate that eliminating the stereocenter by replacing the carbon atom with the nitrogen atom in the structure of **3** is viable.

The next structural change was performed on the 1,2,3-triazole moiety in **I** (Figure 1 and Table 2). The 1,2,3-triazole group is one of the important connecting units in medicinal chemistry due to its several attractive features, such as large dipole moments and stability to metabolic degradation. However, a profound disadvantage of the 1,2,3-triazole compounds is their low aqueous solubility.[12] Parent compound **3** exhibited low aqueous solubility (0.024 mM, as measured by the CheqSol method at 25 °C).[11] Thus, the 1,2,3-triazole moiety was removed and replaced with another functional group. Many types of nonclassical bioisosteres of 1,2,3-triazole are known including amide, isoxazole, and pyrazole. However, we selected a simple alkyl group because it is flexible and not significantly electronically biased. Although alkyl might not be an optimal substituent, this replacement might provide a basis for further optimization. This structural modification resulted in scaffold **II** (Figure 1).

The first series of analogues with scaffold **II** was **II-A** (Table 2), comprising compounds **8**−**11** with piperidine rings and alkyl chain lengths of 2−5 carbon atoms between the two nitrogen atoms. They showed comparable or improved potency in tube formation inhibition compared with that of the parent triazole **4** with a piperidine ring. Furthermore, they were less cytotoxic to the cells. These results suggest that scaffold **II** is a good platform for further optimization.

In a previous study,[11] the modification of the dimethoxyphenyl moiety was not investigated due to its lengthy synthesis. The simplified new structure allowed the rapid synthesis and evaluation of the structure−activity relationship (SAR) around the dimethoxyphenyl moiety (marked as "A" in Figure 1). Several analogues with the generic structure **II-B** were prepared (Table 3). The alkyl chain length of three carbon atoms was adopted because of the higher potency of **9** than other analogues (**8**, **10**, and **11**) with different chain lengths. Removing one methoxy group at the para position yielded analogue **12**, which was found to exhibit a twofold decrease in potency in the inhibition of tube formation. Replacing the two methoxy groups of **9** with two fluoride atoms produced analogue **13** with similar potency. Analogue **14**, with a strong electron-withdrawing trifluoromethyl group, was approximately twofold more active than **9**. However, the replacement of the dimethoxy group resulted in substantially increased cytotoxicity to HUVECs. Analogues with various substituents were also synthesized, but they were not advantageous regarding cytotoxicity (data not shown). With the valuable SAR insights obtained from these studies, we

https://doi.org/10.1021/acs.jmedchem.0c01965
J. Med. Chem. 2021, 64, 5535−5550

advanced to evaluating the amino moiety to identify other opportunities to improve the potency without increasing the cytotoxicity.

Encouraged by the biological results of the generic structure **II-A**, we systematically investigated the influence of the nature and position of the amino moiety (depicted as "B" in Figure 1) on the activity. Additionally, five different amino groups were selected, and a length of 2−5 carbon atoms was adopted. Twenty analogues with the generic structure **II-C** were synthesized in a combinatorial manner. Their activity profiles are shown in Table 4.

No clear relationship could be drawn between the alkyl chain length and activities. However, in general, the increase in chain length resulted in decreased activity against tube formation inhibition. As the chain length increased, the effect on cytotoxicity was increased. These results indicate that these two effects are not correlated. Again, no clear relationship could be drawn between the types of amino groups and activities. Among the tested amino groups, piperidine resulted in a higher level of cytotoxicity and inhibitory potency against tube formation (**8**−**11** vs **15**−**22**). The diethyl amino group-containing compounds (**23**−**26**) exhibited the least cytotoxicity.

Within the series of straight-chain analogues, the most potent molecule to inhibit tube formation was compound **29** with a cyclohexylamino group. However, based on the selectivity index, the cyclopentylamine analogue **31** had more desired biological properties than the other analogues. In contrast to **29**, analogue **31** did not exhibit notable cytotoxicity against HUVECs, showing the highest selectivity index, with potent inhibitory activity (IC_{50} = 2.95 μM) in the tube formation assay.

Chemistry. The synthetic route is outlined in Schemes 1−4. Compound **35** was a fundamental intermediate required for the synthesis of most of the analogues. The synthesis of **35** and its relatives **36**−**38** is shown in Scheme 1. Copper-mediated Chan−Lam coupling of aminothiazole **39**[13] with commercially available phenylboronic acids (**40**−**43**) provided **35**−**38** in modest to good yield.

Scheme 1. Synthesis of Phenylaminothiazolines 35−38[a]

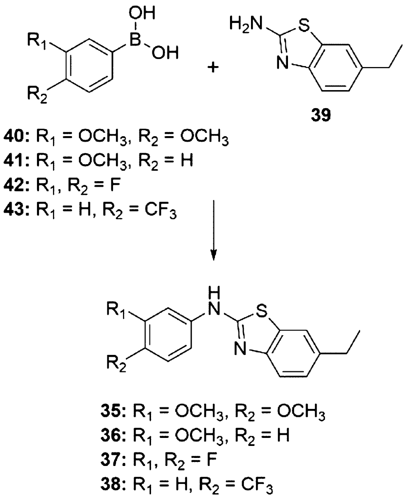

[a]Reagents and conditions: $Cu(OAc)_2$, 2,2′-bipyridine, Cs_2CO_3, DMSO, 70 °C, 14 h, 45−62%.

Scheme 2. Synthesis of 1,2,3-Triazole Analogues 4−7[a]

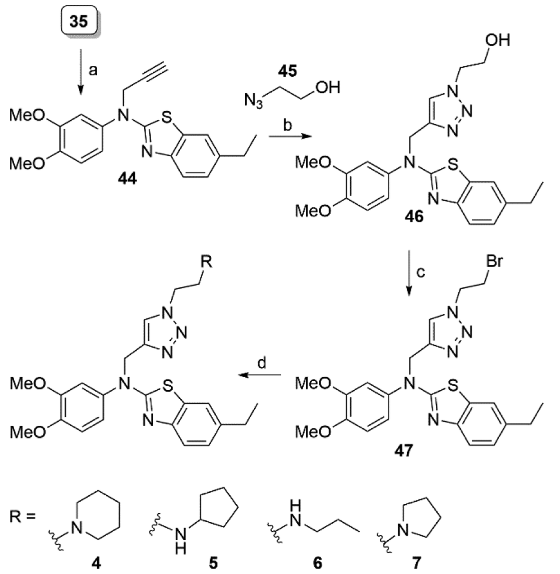

[a]Reagents and conditions: (a) K_2CO_3, propargyl bromide, DMF, 0 °C to rt, 16 h, 92%; (b) $CuSO_4{\cdot}5H_2O$, sodium ascorbate, EtOH/*t*-BuOH/H_2O, 60 °C, 20 min, 87%; (c) CBr_4, PPh_3, CH_2Cl_2, rt, 2 h, 88%; and (d) different amines, K_2CO_3, DMF/MeCN (1:1), 50 °C, 16−19 h, 63−95%.

Scheme 3. Synthesis of Straight-Chain Alkyl Analogues 8−11 and 15−34[a]

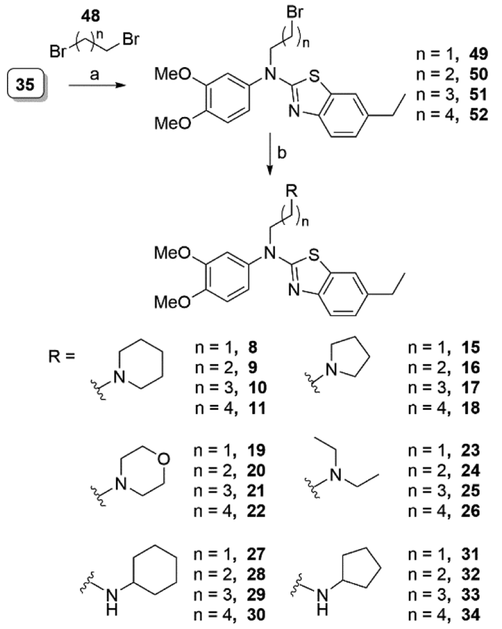

[a]Reagents and conditions: (a) NaH, DMF, 50 °C, 13 h, 53−79% and (b) different amines, K_2CO_3, DMF/MeCN (1:1), 50 °C, 12−18 h, 37−98%.

The synthesis of 1,2,3-triazole analogues (**4**−**7**) started with the alkylation of **35** with propargyl bromide to produce **44** (Scheme 2). 1,3-Dipolar cycloaddition of alkyne **44** and azide **45**[14] in the presence of a catalytic amount of Cu salt produced 1,2,3-triazole intermediate **46**, which was converted to bromide **47** via an Appel reaction. The resulting bromide **47** reacted

Scheme 4. Synthesis of Straight-Chain Alkyl Analogues 12–14 with Modification on the Phenyl Moiety[a]

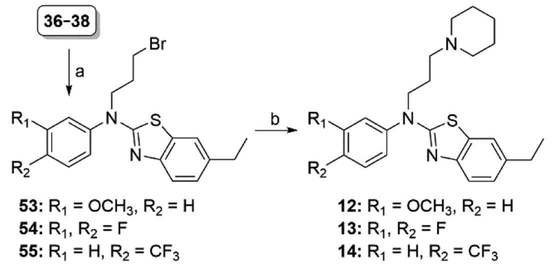

[a] Reaction conditions: (a) 1,3-dibromo-propane, NaH, DMF, 50 °C, 14 h, 54–70% and (b) piperidine, K_2CO_3, DMF/MeCN, 50 °C, 14–16 h, 42–56%.

with various amines to generate the corresponding amino-substituted 1,2,3-triazole analogues (**4**–**7**).

Straight-chain analogues (**8**–**11** and **15**–**34**) were synthesized using **35** as the starting material (Scheme 3). The alkylation of **35** with dibromoalkanes **48** in the presence of NaH provided bromides **49**–**52**. The obtained **49**–**52** were converted into amino-substituted analogues (**8**–**11** and **15**–**34**) through nucleophilic substitution with various amines.

As shown in Scheme 4, the synthesis of analogues **12**–**14** with a modified phenyl moiety started with the alkylation of the corresponding aminothiazole **36**–**38** with 1,3-dibromopropane to produce **53**–**55**. The resulting bromides **53**–**55** were treated with piperidine and K_2CO_3 to produce the corresponding piperidine-substituted analogues **12**–**14**, respectively.

Preliminary Pharmaceutical Properties of Compound 31. To assess the basic pharmaceutical properties of **31**, the aqueous solubility, plasma stability, and metabolic stability were examined (Table 5). Compared with its parent compound **3**, a notable property of **31** is its higher aqueous solubility, probably due to removing the 1,2,3-triazole moiety. The aqueous solubility of **31** increased approximately 10 times (0.21 mM, as measured by the CheqSol method at 25 °C). Compound **31** showed excellent plasma stability with >99% remaining after 30 min incubation with human plasma. In the metabolic stability study using human liver microsomes, good microsomal stability was also observed.

Table 5. Preliminary ADME Study of 31

compd	pK_a	solub (mM)[a]	plasma stability (%)[b]	microsomal stability (%)[c]
3[d]	9.24	0.024	95	31
31	11.9	0.21	107.1 ± 1.8 (2)	52.2 ± 2.3 (2)

[a] Measured by the CheqSol method at 25 °C. [b] Percentage of the compound remaining after 30 min in human plasma. The number of replicates is in parentheses. [c] Percentage of the compound remaining after 120 min in human liver. The number of replicates is in parentheses. [d] The data were taken from ref 11 for comparison.

Evaluation of Antiangiogenic Activity and Cytotoxicity of 31. The tube formation activity and cell viability of **31** were compared with those of sunitinib. The calculated IC_{50} values for VEGF-induced tube formation were 2.95 ± 0.59 for **31** and 2.54 ± 0.6 for sunitinib in HUVEC cells. Under the same experimental conditions, the two compounds showed similar inhibitory activity against tube formation induced by VEGF (Figure 2A), while **31** exhibited much lower cytotoxicity against HUVECs and HRMECs (Figure S5). The calculated selectivity index values for **31** and sunitinib were 33.9 and 3.9, respectively (Figure 2B). Although sunitinib is a potent vascular endothelial growth factor receptor 2 (VEGFR2) kinase inhibitor, its inhibitory effects against tube formation were largely due to cytotoxicity.

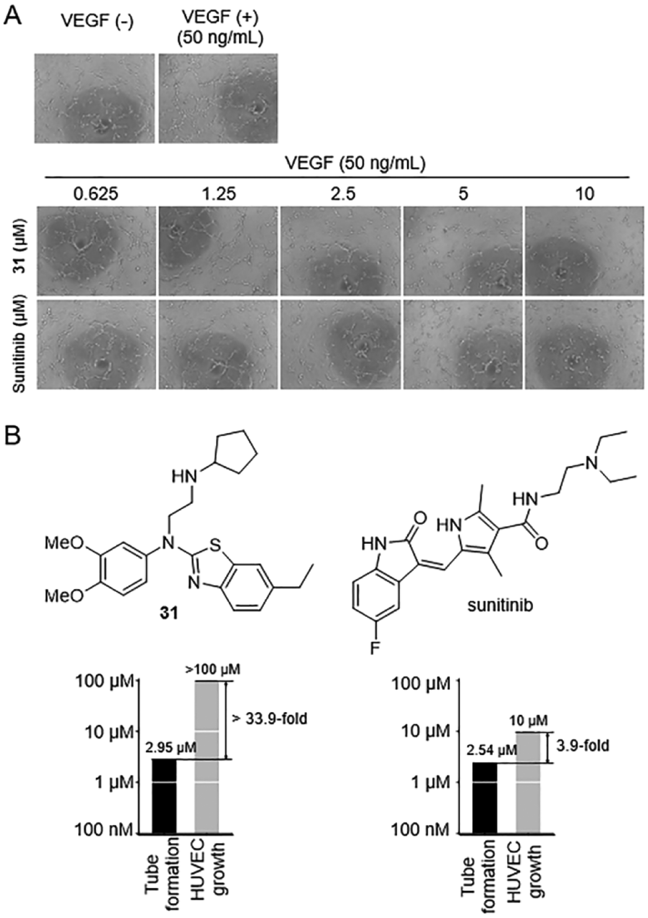

Figure 2. (A) VEGF-induced tube formation on Matrigel in HUVECs. (B) Chemical structures of **31** and sunitinib and their effects on VEGF-induced tube formation and cell viability in HUVECs.

Compound 31 Inhibits *p*-VEGFR2 Expression and Cell Migration in HUVECs. Our structural modification provided meaningful insights into the SAR of this class of compounds and complexity-reduced, drug-like scaffold with antiangiogenic activity without apparent cytotoxicity against HUVECs. Further biological studies were performed with compound **31** to understand the precise molecular mechanism of action and evaluate the antiangiogenic activity in *in vivo* animal models. VEGF binds to VEGFR2 and activates the downstream signaling pathway, which plays a major role in angiogenesis.[15] Therefore, the effect of **31** on *p*-VEGFR2 expression was evaluated using Western blot analysis in HUVECs. VEGF (50 ng/mL) induced the expression of *p*-VEGFR2, and **31** effectively suppressed the phosphorylation of VEGFR2 in a concentration-dependent manner without impacting VEGFR2 expression (Figure 3A). Compound **31** showed mild inhibitory activity in direct VEGFR-2 kinase assay, indicating the existence of alternative molecular mechanism regulated by **31** independent of VEGFR2 kinase activity (Figure S6). Additionally, KINOMEscan kinase-small

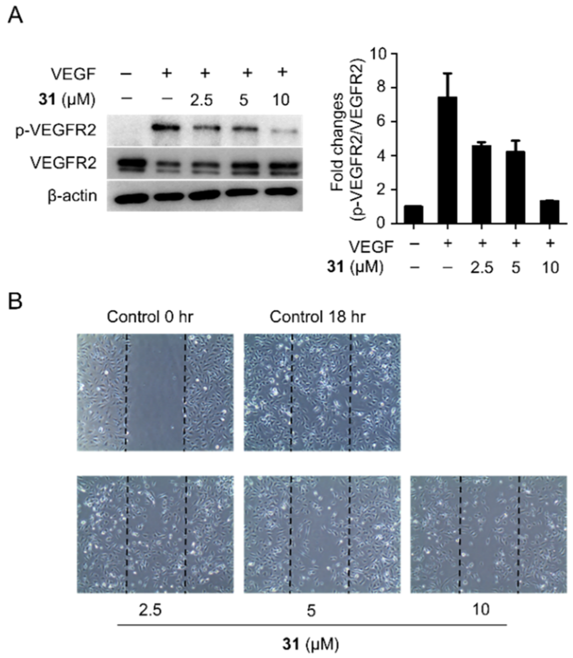

Figure 3. (A) After cells reached 90% confluency, HUVECs were starved overnight, and the medium was changed to endothelial basal medium (EBM) containing 2% fetal bovine serum (FBS). **31** was pretreated for 30 min, followed by VEGF (50 ng/mL) treatment for 30 min. Western bands were quantified using ImageJ, and then, we calculated the relative intensity. The data are presented as the mean fold changes ± SD of two independent experiments. (B) Scratches were induced in HUVECs, and the medium was changed to EBM containing 2% FBS. Dimethyl sulfoxide (DMSO) or indicated concentrations of **31** were treated for 18 h, and the cells were photographed using microscopy.

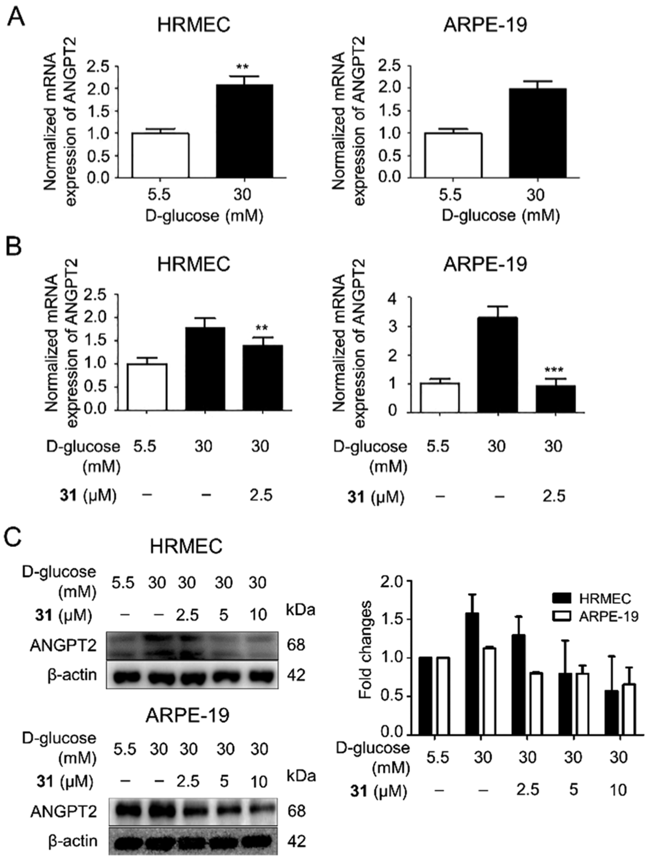

Figure 4. Effects of **31** on ANGPT2 expression induced by high glucose in HRMECs and ARPE-19 cells. (A) HRMECs and ARPE-19 cells were stimulated with D-glucose for 48 h. The level of ANGPT2 gene expression was analyzed by real-time PCR. The cells were pretreated with **31** for 30 min and further incubated with D-glucose (30 mM) for 48 h. The expression levels of ANGPT2 gene and protein were analyzed by (B) real-time PCR and (C) Western blotting analysis, respectively. Western bands were quantified using ImageJ and presented as the mean fold changes ± SD of two independent experiments. Real-time PCR data are presented as the mean fold changes ± SD of three independent experiments. ($^{*}P < 0.05$, $^{**}P < 0.01$, and $^{***}P < 0.005$).

molecule binding assay was performed against 468 kinases, and no significant inhibition of kinase activity was observed (Table S1). The effect of **31** on cell migration, which is a fundamental process in angiogenesis,[16] was assessed using scratch migration assay. **31** inhibited cell migration without affecting cell viability and morphology (Figure 3B).

Compound 31 Suppresses ANGPT2 Expression Induced by D-Glucose. ANGPT2 is a ligand of the tunica interna endothelial cell kinase 2 (TIE2) receptor, which is involved in vascular remodeling, pericyte dropout, and neovascularization.[17−19] Patient data suggest that the expression of ANGPT2 is higher in eyes with retinal detachment than in those with a completely attached retina, and the levels of ANGPT2 are associated with upregulated expression of MMP-9, VEGF, and TGFβ1.[5] Cells were incubated with high glucose to mimic diabetic conditions. We found that high glucose (30 mM) treatment for 48 h induced ANGPT2 expression in both HRMECs and ARPE19 cells (Figure 4A). Treatment with **31** significantly suppressed the ANGPT2 gene expression induced by high glucose (Figure 4B). Additionally, **31** suppressed the protein expression of ANGPT2 in a concentration-dependent manner in both HRMECs and ARPE-19 cells (Figure 4C). Crosstalk occurs between ANGPT2 and VEGF, synergistically increasing vascular permeability in diabetic macular edema (DME).[20] Currently, anti-ANGPT2 monoclonal antibodies are under investigation to treat wet age-related macular degeneration (AMD), DME, and cancer.[21−23] Although small-molecule Tie-2 kinase inhibitors are available to regulate ANGPT2/Tie2 signaling, their efficacy has only been examined for cancer treatment.[24,25] Recent clinical data suggest that patients with DME treated with bispecific antibodies targeting both ANGPT2 and VEGF-A show better outcomes than DME patients treated with ranibizumab, an antibody targeting VEGF-A.[26] Compound **31** is a potent inhibitor of VEGF-stimulated *p*-VEGFR2 expression and high glucose-induced ANGPT2 expression, which are highly associated with the angiogenesis of retinopathic processes. These data suggest that **31** has the potential to have superior efficacy over drugs with a single target.

Compound 31 Modulates the c-Abl/STAT5/PI3K Pathway. To investigate the molecular mechanism of **31**, protein interaction network analysis of ANGPT2 was performed using STRING v.11 (Figure 5A).[27] STRING analysis provides information on both the physical and functional associations of different proteins. The protein network analysis suggests that ANGPT2 is associated with TEK Receptor tyrosine kinase (TEK/Tie-2), signal transducer and activator of transcription 5A (STAT5A), STAT5B, phosphatidylinositol-4,5-bisphosphate 3-kinase catalytic sub-

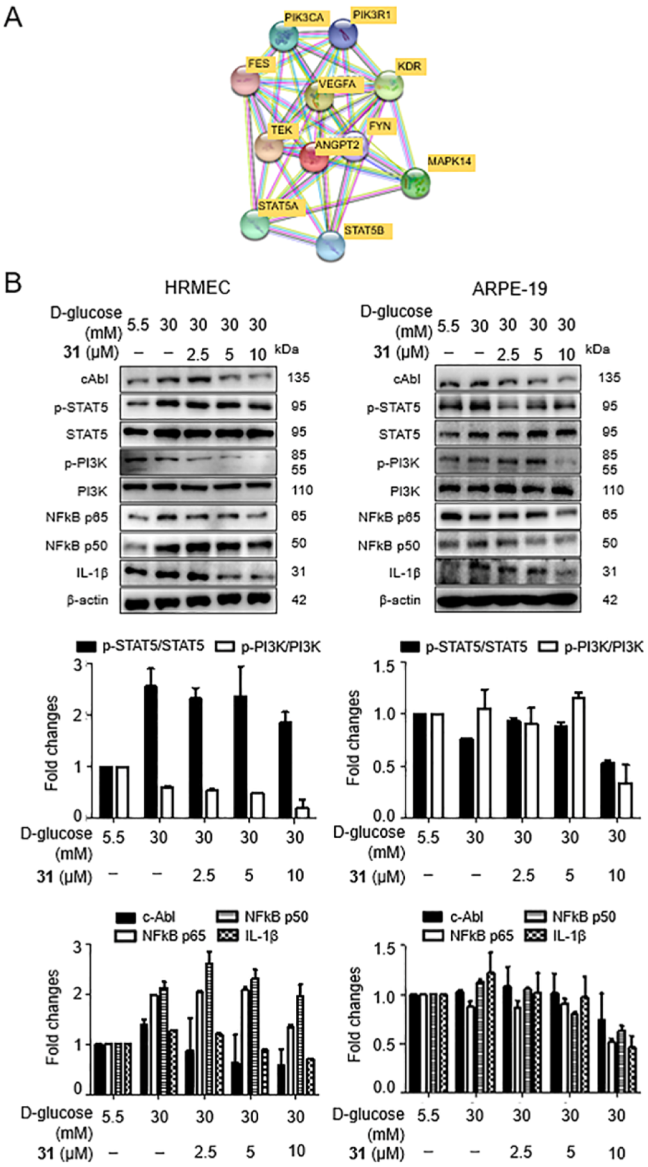

Figure 5. (A) Protein interaction network analysis associated with ANGPT2 was performed using STRING v.11. (B) Cells were pretreated with **31** for 30 min and incubated with the indicated concentration of D-glucose for 48 h. The effects of **31** on ANGPT2-linked biomarker expression were evaluated by Western blot analysis in D-glucose-stimulated HRMECs and ARPE-19 cells. Western bands were quantified using ImageJ and presented as the mean fold changes ± SD of two independent experiments.

unit alpha (PIK3CA), phosphatidylinositol 3-kinase regulatory subunit alpha (PIK3R1), tyrosine-protein kinase Fes/Fps (FES), kinase insert domain receptor (KDR/VEGFR2), tyrosine-protein kinase Fyn (FYN), vascular endothelial growth factor A (VEGFA), and mitogen-activated protein kinase 14 (MAPK14). In particular, STAT5 promotes angiogenesis, and its expression is increased in the retina of diabetic rats compared with that in normal rats.[28−30] Phosphatidylinositol 3-kinase (PI3K) regulates various proangiogenic factors and is involved in the migration activity of endothelial cells.[31,32] High glucose induced c-Abl, phosphorylation of STAT5, and PI3K in HRMEC cells but not in ARPE19 cells, which suggests that two cell lines may have different sensitivities to glucose. Treatment with **31** suppressed p-STAT5 and p-PI3K expression in a concentration-dependent manner without suppressing total expressions of STAT5 and PI3K (Figure 5B). In addition, abelson tyrosine kinase (c-Abl), which regulates STAT5[33] and PI3K,[34] was also downregulated by **31**. Increased levels of cytokines and proinflammatory biomarkers are positively correlated with the progression of angiogenesis in diabetic retinopathy patients.[35−37] Treatment with **31** inhibited proinflammatory biomarkers induced by high glucose, such as nuclear factor kappa-light-chain-enhancer of activated B cells (NFκB) p50, NFκB p65, and interleukin 1 beta (IL-1β) (Figure 5B). These data suggest that the molecular mechanism of **31** is associated, in part, with the suppression of the c-Abl/STAT5/PI3K signaling pathway.

Intravitreal Injection of Compound 31 Ameliorates Pathological Retinal Neovascularization in the OIR Mouse Model. VEGF and its receptors exert key roles in pathological neovascularization in various diseases. In retinopathy of prematurity (ROP) and proliferative diabetic retinopathy (PDR), VEGF and its receptors have been recognized as main disease targets in that enhanced VEGF signaling induces the excessive growth of a leaky retinal vasculature, leading to vision impairment and loss. Thus, we determined the effect of **31** on pathological neovascularization in the retina using an OIR model, a common animal model of ROP and PDR. Newborn mice were exposed to 75% oxygen from P7 to P12. At P12, they were returned to a room with normal air and received intravitreal administration of **31** and DMSO (control vehicle). At P17, the extent of neovascularization was assessed by quantifying the formation of neovascular tufts, reflecting pathological retinal neovascularization (Figure 6A). Although DMSO-injected eyes displayed pronounced tuft formation in the retina, the eyes of **31**-injected mice exhibited a significant decrease in retinal neovascularization. These results indicate that **31** efficiently blocks VEGF-induced pathological retinal neovascularization in mice with OIR.

Compound 31 Ameliorates Pathologic Neovascularization in the CNV Mouse Model. To evaluate the antiangiogenic efficacy of **31**, a mouse laser-induced CNV model was employed. The efficacy of **31** was determined by eye drop formulation. Fundus fluorescein angiography (FFA) was photographed 10 days after CNV induction. In the CNV lesion size observed on FFA, a statistically significant decrease was observed in the test group-administered 1% **31** compared with that in the vehicle group ($P < 0.05$). Additionally, the effects were similar to those of the test group-administered aflibercept (Eylea) ($P < 0.05$) (Figure 7A).

The cross-sectional view of the retina was photographed using optical coherence tomography angiography (OCTA) 10 days after CNV induction. However, comparing the volume of the lesion on OCTA with that of the vehicle group, the lesion volume was significantly reduced in the test group-administered 1% **31** ($P < 0.05$). However, efficacy was not superior to that of the test group-administered aflibercept (Eylea) ($P < 0.0001$) (Figure 7B). The scotopic retinal potential test (ERG) response was measured at a light intensity of 0.9 log cds/m^2 11 days after CNV induction. The highest retinal potential was observed in the aflibercept (Eylea) administration group ($P < 0.0001$), and the 1% **31** administration group showed more significant increases than the vehicle administration group ($P < 0.05$) (Figure 7C).

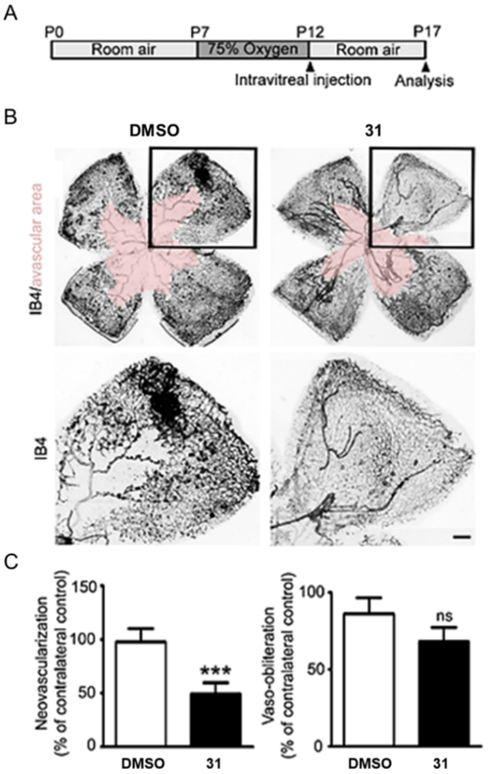

Figure 6. (A) Schematic diagram of OIR experiments. At P12, mice received a single intravitreal injection of **31** (3 μg in 1 μL DMSO) or DMSO (1 μL). Five days later (P17), the eyes were harvested for further analysis. (B) Representative images of whole-mounted retinas of mice with OIR at P17. The retinal vasculature was visualized by staining with isolectin B4 (IB4; black). High-magnification views of the boxed areas are shown at the bottom. Scale bars = 100 μm. (C) Retinal neovascularization and vaso-obliteration in mice with OIR were quantified as a percentage of the number of pixels in the neovascular tuft and avascular regions of retinas with intravitreal injections compared to those of uninjected contralateral controls, respectively. Data are presented as the mean ± SEM (***$P < 0.001$, ns = not significant, $n > 6$ mice per group).

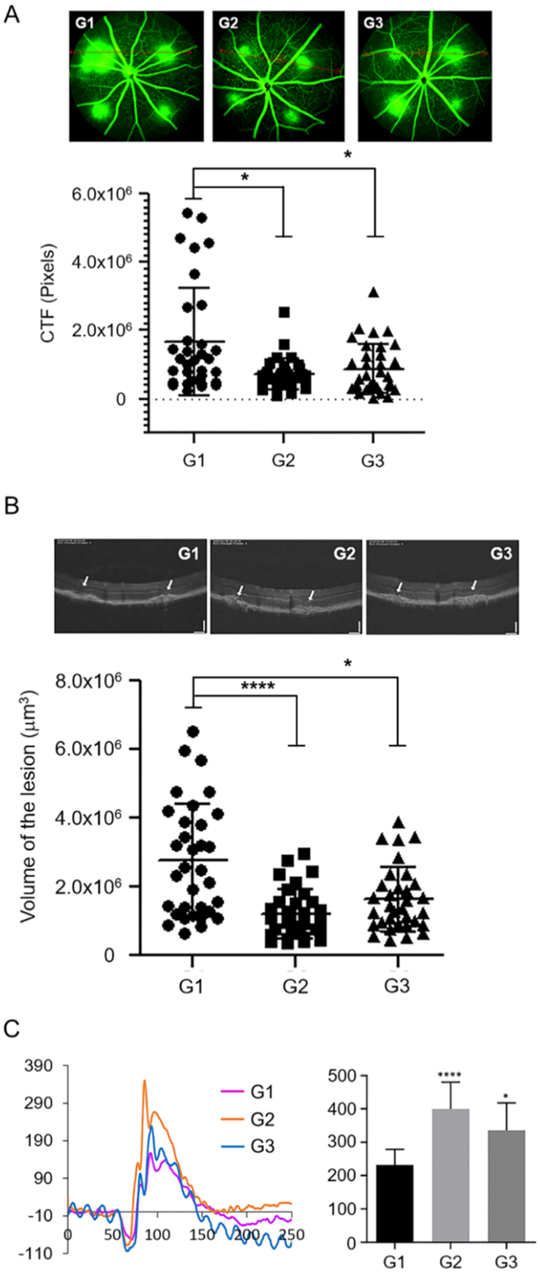

Figure 7. Representative FFA images and corrected total fluorescence (CTF) at 10 days after CNV induction. (A) The CTF of the wounded area was analyzed by ImageJ. Each group was assigned as follows: G1 (CNV control: vehicle, eye drops, $n = 33$); G2 (Eylea, IVT, $n = 32$); and G3 (**31**, 1%, eye drops, $n = 34$). Three groups of mice ($n = 5$) were studied and compared with G1 (vehicle). (B) White arrows indicate CNV lesions. The volume of the lesions was measured using ImageJ. Each group was assigned as follows: G1 (CNV control: vehicle, eye drops, $n = 33$); G2 (Eylea, IVT, $n = 32$); and G3 (**31**, 1%, eye drops, $n = 34$). Three groups of mice ($n = 5$) were studied and compared with G1 (vehicle). (C) Amplitude of each eye was analyzed using "LabScribeERG Software". Each group was assigned as follows: G1 (CNV control: vehicle, eye drops, $n = 10$); G2 (Eylea, IVT, $n = 8$); and G3 (**31**, 1%, eye drops, $n = 8$). Three groups of mice ($n = 5$) were studied and compared with G1 (vehicle) (*$P < 0.05$, **$P < 0.01$, and ****$P < 0.0001$).

■ CONCLUSIONS

VEGF is a major proangiogenic mediator that plays an important role in the development of neovascularized pathogenic processes. Therefore, anti-VEGF biologics are currently used in the clinic to treat diabetic retinopathy to inhibit abnormal vessel growth caused by high glucose blood levels in the eye environment. However, current anti-VEGF biologic drugs have limitations, including the lack of long-lasting effects, frequent intravitreal injections, and the generation of side effects. Therefore, the development of novel, safe, and potent antiangiogenic small molecules may provide a crucial benefit to complement biologic therapy. Additionally, ANGPT2 is involved in neovascularization and ANGPT2 overexpression occurs in retinal pathogenic processes. In particular, high glucose potentially upregulates ANGPT2 expression and subsequently increases vascular permeability in the retina. ANGPT2 is also upregulated by VEGF, suggesting crosstalk between ANGPT2 and VEGF in the progression of diabetic retinopathy. In this study, we designed and synthesized structurally simplified wondonin analogues starting from previously developed **3** with an epimerizable chiral center. The initial structural modification of parent compound **3** was performed by eliminating the stereocenter by replacing the carbon atom with the nitrogen atom. The next structural change was the replacement of the triazole ring with the simple alkyl chain. This modification yielded a compound that had improved potency in tube formation inhibition and less cytotoxicity compared to the parent triazole compound. In general, the decrease in alkyl chain length resulted in increased potency and decreased cytotoxicity. No clear relationship was drawn between the types of pendant amino groups and activities. The modification of the dimethoxyphenyl moiety was not tolerated. Through SAR studies, we identified analogue **31**, which exhibits potent antiangiogenic activity with minimized cytotoxicity in HUVEC. The selectivity index value of **31** was higher than that of **3** or sunitinib, and the aqueous solubility of **31** was higher than that of **3**. Compound **31** effectively suppressed the activation of VEGF-induced VEGFR2 expression (*p*-VEGFR2) and high glucose-induced ANGPT2 expression. Further molecular mechanism studies revealed that ANGPT2 suppression by **31** is associated with the modulation of the c-Abl/STAT5/PI3K pathway in ocular cells. The *in vivo* antiangiogenic activity of **31** was also demonstrated in CNV and OIR mouse models. Our data collectively suggest that compound **31** is prioritized as a promising lead or candidate to develop small-molecule therapeutic agents to treat diabetic retinopathy.

■ EXPERIMENTAL SECTION

Chemistry. The details of the synthesis procedures, including all the intermediates and analogues **4**−**34**, are described in the Supporting Information. All the chemicals used were purchased in reagent grade from commercial suppliers, and all the reactions were executed under an inert atmosphere comprising dry nitrogen using distilled dry solvents. The reactions were monitored by thin-layer chromatography (TLC) performed on silica gel 60 F_{254} TLC plates. The synthesized products were purified by flash column chromatography on silica gel 60 (40−63 μm, 230−400 mesh, Merck). NMR spectra were recorded using a JNM-ECZ400S/L1 spectrometer (Jeol, Akishima, Tokyo, Japan). ^{1}H NMR (400 MHz) and ^{13}C NMR (100 MHz) spectra were obtained in δ units using residual $CDCl_3$ (^{1}H NMR δ = 7.26 ppm and ^{13}C NMR δ = 77.16 ppm) and CD_2Cl_2 (^{1}H NMR δ = 5.32 ppm and ^{13}C NMR δ = 53.84 ppm) as the internal standards. IR spectra were obtained using an Agilent 5500a FTIR system (Agilent, USA). High-resolution mass spectroscopy (HRMS) spectra were obtained using fast atom bombardment (FAB) and electrospray ionization (ESI). The purity of all the final target compounds was confirmed to be at least >95% pure by analytical HPLC (Agilent 1200 Series; Agilent Technologies, Palo Alto, CA, USA). The purity of all the final target compounds, HPLC methods, and spectra are shown in the Supporting Information.

***N*-(3,4-Dimethoxyphenyl)-6-ethyl-*N*-((1-(2-(piperidin-1-yl)-ethyl)-1*H*-1,2,3-triazol-4-yl)methyl)benzo[*d*]thiazol-2-amine (4).** To a solution of **47** (100 mg, 0.20 mmol) in DMF/MeCN (1:1, 2 mL, 0.1 M) was added K_2CO_3 (110 mg, 0.80 mmol) and piperidine (200 μL, 1.99 mmol). The reaction mixture was stirred at 50 °C for 19 h and then diluted with H_2O and extracted with ethyl acetate (EtOAc). The organic layer was dried over $MgSO_4$, filtered, and evaporated *in vacuo*. The crude product was separated by silica gel column chromatography (CH_2Cl_2/MeOH, 30:1, R_f = 0.2) to produce the desired product **4** (96.0 mg, 95%, ivory solid). ^{1}H NMR (400 MHz, $CDCl_3$): δ 7.96 (s, 1H), 7.15 (d, J = 8.0 Hz, 1H), 7.11−7.08 (m, 1H), 7.01 (d, J = 2.0 Hz, 1H), 6.96−6.93 (m, 1H), 6.90 (d, J = 8.3 Hz, 1H), 6.74−6.73 (m, 1H), 4.74 (s, 2H), 4.46 (t, J = 6.2 Hz, 2H), 3.92 (s, 3H), 3.86 (s, 3H), 2.75 (t, J = 6.2 Hz, 2H), 2.50−2.41 (m, 6H), 1.60−1.54 (m, 4H), 1.45−1.40 (m, 2H), 1.08 (t, J = 7.6 Hz, 3H); ^{13}C NMR (100 MHz, $CDCl_3$): δ 150.0, 149.8, 145.5, 141.6, 136.4, 134.9, 128.7, 127.6, 126.7, 126.6, 124.1, 122.4, 117.2, 115.5, 112.0, 58.3, 56.3, 56.1, 54.7 (2C), 49.5, 48.1, 28.6, 26.1 (2C), 24.3, 15.4; IR (neat) υ_{max}: 2933, 2214, 1584, 1503, 1440, 1253, 1230, 1135, 1022, 807, 762 (cm^{-1}); HRMS (FAB): calcd for $C_{27}H_{35}N_6O_2S$ [M + H]$^+$, 507.2542; found, 507.2539.

All **5**−**7** compounds were synthesized using a similar procedure to that for compound **4**.

***N*-((1-(2-(Cyclopentylamino)ethyl)-1*H*-1,2,3-triazol-4-yl)-methyl)-*N*-(3,4-dimethoxyphenyl)-6-ethylbenzo[*d*]thiazol-2-amine (5).** (90.0 mg, 89%, yellow oil). ^{1}H NMR (400 MHz, $CDCl_3$): δ 7.86 (s, 1H), 7.16 (d, J = 8.0 Hz, 1H), 7.09−7.06 (m, 1H), 6.99 (d, J = 2.1 Hz, 1H), 6.95−6.92 (m, 1H), 6.89 (d, J = 8.3 Hz, 1H), 6.73−6.72 (m, 1H), 4.72 (s, 2H), 4.45 (t, J = 5.9 Hz, 2H), 3.90 (s, 3H), 3.84 (s, 3H), 3.09−3.03 (m, 3H), 2.46 (q, J = 7.6 Hz, 2H), 1.81−1.75 (m, 2H), 1.66−1.58 (m, 2H), 1.52−1.46 (m, 3H), 1.29−1.21 (m, 2H), 1.07 (t, J = 7.6 Hz, 3H); ^{13}C NMR (100 MHz, $CDCl_3$): δ 150.0, 149.7, 145.5, 141.6, 136.3, 134.8, 128.7, 127.6, 126.62, 126.56, 124.0, 122.3, 117.1, 115.3, 112.0, 59.6, 56.2, 56.1, 51.1, 49.3, 47.8, 33.2 (2C), 28.5, 24.0 (2C), 15.4; IR (neat) υ_{max}: 2954, 2852, 2214, 1584, 1503, 1398, 1253, 1230, 1022, 762 (cm^{-1}); HRMS (FAB): calcd for $C_{27}H_{35}N_6O_2S$ [M + H]$^+$, 507.2542; found, 507.2552.

***N*-(3,4-Dimethoxyphenyl)-6-ethyl-*N*-((1-(2-(propylamino)-ethyl)-1*H*-1,2,3-triazol-4-yl)methyl)benzo[*d*]thiazol-2-amine (6).** (70.0 mg, 73%, white solid). ^{1}H NMR (400 MHz, $CDCl_3$): δ 7.86 (s, 1H), 7.16 (d, J = 8.0 Hz, 1H), 7.08 (dd, J = 8.2, 2.1 Hz, 1H), 6.99 (d, J = 2.0 Hz, 1H), 6.94 (dd, J = 8.0, 1.9 Hz, 1H), 6.88 (d, J = 8.4 Hz, 1H), 6.72−6.71 (m, 1H), 4.72 (s, 2H), 4.45 (t, J = 5.9 Hz, 2H), 3.90 (s, 3H), 3.84 (s, 3H), 3.09 (t, J = 5.9 Hz, 2H), 2.56 (t, J = 7.2 Hz, 2H), 2.46 (q, J = 7.6 Hz, 2H), 1.49−1.40 (m, 3H), 1.07 (t, J = 7.6 Hz, 3H), 0.87 (t, J = 7.4 Hz, 3H); ^{13}C NMR (100 MHz, $CDCl_3$): δ 150.0, 149.7, 145.5, 141.6, 136.3, 134.8, 128.6, 127.6, 126.63, 126.55, 124.0, 122.3, 117.1, 115.3, 112.0, 56.2, 56.1, 51.4, 50.7, 49.3, 49.0, 28.5, 23.2, 15.4, 11.8; IR (neat) υ_{max}: 2927, 2214, 1584, 1503, 1440, 1253, 1230, 1138, 1022, 763 (cm^{-1}); HRMS (ESI): calcd for $C_{25}H_{33}N_6O_2S$ [M + H]$^+$, 481.2380; found, 481.2387.

***N*-(3,4-Dimethoxyphenyl)-6-ethyl-*N*-((1-(2-(pyrrolidin-1-yl)-ethyl)-1*H*-1,2,3-triazol-4-yl)methyl)benzo[*d*]thiazol-2-amine (7).** (62.0 mg, 63%, ivory solid). ^{1}H NMR (400 MHz, $CDCl_3$): δ 7.89 (s, 1H), 7.14 (d, J = 8.0 Hz, 1H), 7.10−7.07 (m, 1H), 7.00 (d, J = 2.0 Hz, 1H), 6.95−6.93 (m, 1H), 6.89 (d, J = 8.3 Hz, 1H), 6.73−6.72 (m, 1H), 4.73 (s, 2H), 4.49 (t, J = 6.4 Hz, 2H), 3.91 (s, 3H), 3.85 (s, 3H), 2.95 (t, J = 6.4 Hz, 2H), 2.56−2.52 (m, 4H), 2.47 (q, J = 7.6 Hz, 2H), 1.81−1.74 (m, 4H), 1.08 (t, J = 7.6 Hz, 3H); ^{13}C NMR (100 MHz, $CDCl_3$): δ 150.0, 149.8, 145.5, 141.7, 136.3, 134.8, 128.7, 127.6, 126.7, 126.6, 123.9, 122.4, 117.1, 115.5, 112.0, 56.2, 56.1, 55.5, 54.2 (2C), 49.7, 49.4, 28.5, 23.7 (2C), 15.4; IR (neat) υ_{max}: 2962, 2798, 2214, 1584, 1503, 1398, 1253, 1230, 1137, 1022, 763 (cm^{-1}); HRMS (FAB): calcd for $C_{26}H_{33}N_6O_2S$ [M + H]$^+$, 493.2386; found, 493.2382.

***N*-(3,4-Dimethoxyphenyl)-6-ethyl-*N*-(2-(piperidin-1-yl)-ethyl)benzo[*d*]thiazol-2-amine (8).** To a solution of **49** (150 mg, 0.36 mmol) in DMF/MeCN (1:1, 3.56 mL, 0.1 M) was added K_2CO_3 (197 mg, 1.42 mmol) and piperidine (352 μL, 3.56 mmol). The reaction mixture was stirred at 50 °C for 13 h and then diluted with H_2O and extracted with EtOAc. The organic layer was dried over $MgSO_4$, filtered, and evaporated *in vacuo*. The crude product was separated by silica gel column chromatography (CH_2Cl_2/MeOH, 20:1, R_f = 0.2) to produce the desired product **8** (90.0 mg, 59%, white solid). ^{1}H NMR (400 MHz, $CDCl_3$): δ 7.32 (d, J = 8.0 Hz, 1H), 7.09−7.07 (m, 1H), 7.00−6.96 (m, 2H), 6.89 (d, J = 8.3 Hz, 1H), 6.71−6.72 (m, 1H), 3.91 (s, 3H), 3.85 (s, 3H), 3.55 (t, J = 6.8 Hz, 2H), 2.61 (t, J = 6.8 Hz, 2H), 2.51−2.41 (m, 6H), 1.60−1.54 (m, 4H), 1.45−1.41 (m, 2H), 1.09 (t, J = 7.6 Hz, 3H); ^{13}C NMR (100 MHz, $CDCl_3$): δ 150.0, 149.7, 145.1, 136.4, 135.2, 128.4, 127.6, 127.1, 126.3, 122.5, 117.2, 116.0, 112.0, 56.24, 56.21, 56.1, 54.7 (2C), 51.0, 28.5, 26.0 (2C), 24.4, 15.5; IR (neat) υ_{max}: 2934, 2214, 1584, 1503, 1398, 1253, 1231, 1135, 1023, 762 (cm^{-1}); HRMS (ESI): calcd for $C_{24}H_{32}N_3O_2S$ [M + H]$^+$, 426.2210; found, 426.2204.

All **9**−**11** and **15**−**34** compounds were synthesized using a similar procedure to that for compound **8**.

***N*-(3,4-Dimethoxyphenyl)-6-ethyl-*N*-(3-(piperidin-1-yl)-propyl)benzo[*d*]thiazol-2-amine (9).** (102 mg, 68%, ivory solid). ^{1}H NMR (400 MHz, $CDCl_3$): δ 7.23 (d, J = 8.0 Hz, 1H), 7.09 (dd, J = 8.3, 2.1 Hz, 1H), 7.00−6.97 (m, 2H), 6.90 (d, J = 8.4 Hz, 1H), 6.71−6.70 (m, 1H), 3.92 (s, 3H), 3.85 (s, 3H), 3.49 (t, J = 7.3 Hz, 2H), 2.50−2.39 (m, 8H), 2.00−1.92 (m, 2H), 1.60−1.54 (m, 4H), 1.45−1.42 (m, 2H), 1.09 (t, J = 7.6 Hz, 3H); ^{13}C NMR (100 MHz, CDCl$_3$): δ 150.0, 149.8, 145.2, 136.6, 135.2, 128.5, 127.7, 126.4 (2C), 122.4, 117.2, 115.8, 112.0, 56.2, 56.1, 55.8, 54.6 (2C), 52.4, 28.6, 26.0 (2C), 25.3, 24.5, 15.5; IR (neat) υ_{max}: 2933, 2213, 1584, 1503, 1400, 1252, 1230, 1136, 1023, 851, 762 (cm^{-1}); HRMS (ESI): calcd for $C_{25}H_{34}N_3O_2S$ [M + H]$^+$, 440.2366; found, 440.2370.

***N*-(3,4-Dimethoxyphenyl)-6-ethyl-*N*-(4-(piperidin-1-yl)butyl)benzo[*d*]thiazol-2-amine (10).** (87.0 mg, 66%, yellow oil). ^{1}H NMR (400 MHz, CDCl$_3$): δ 7.20 (d, J = 8.0 Hz, 1H), 7.06 (dd, J = 8.2, 2.1 Hz, 1H), 6.98−6.95 (m, 2H), 6.88 (d, J = 8.4 Hz, 1H), 6.69−6.68 (m, 1H), 3.90 (s, 3H), 3.83 (s, 3H), 3.43 (t, J = 7.1 Hz, 2H), 2.49−2.39 (m, 8H), 1.81−1.60 (m, 8H), 1.46−1.43 (m, 2H), 1.07 (t, J = 7.6 Hz, 3H); ^{13}C NMR (100 MHz, CDCl$_3$): δ 150.0, 149.7, 145.2, 136.5, 135.1, 128.4, 127.7, 126.4, 126.3, 122.2, 117.2, 115.7, 112.0, 58.6, 56.2, 56.0, 54.4 (2C), 53.8, 28.5, 26.0, 25.5 (2C), 24.1, 23.4, 15.4; IR (neat) υ_{max}: 2935, 2213, 1584, 1503, 1441, 1253, 1230, 1136, 1023, 728 (cm^{-1}); HRMS (ESI): calcd for $C_{26}H_{36}N_3O_2S$ [M + H]$^+$, 454.2523; found, 454.2527.

***N*-(3,4-Dimethoxyphenyl)-6-ethyl-*N*-(5-(piperidin-1-yl)pentyl)benzo[*d*]thiazol-2-amine (11).** (109 mg, 83%, ivory solid). ^{1}H NMR (400 MHz, CDCl$_3$): δ 7.20 (d, J = 8.0 Hz, 1H), 7.08 (dd, J = 8.2, 2.1 Hz, 1H), 6.99−6.96 (m, 2H), 6.89 (d, J = 8.3 Hz, 1H), 6.70 (d, J = 2.0 Hz, 1H), 3.91 (s, 3H), 3.85 (s, 3H), 3.41 (t, J = 7.4 Hz, 2H), 2.50−2.36 (m, 8H), 1.82−1.75 (m, 2H), 1.67−1.56 (m, 6H), 1.48−1.40 (m, 4H), 1.08 (t, J = 7.6 Hz, 3H); ^{13}C NMR (100 MHz, CDCl$_3$): δ 150.0, 149.8, 145.2, 136.6, 135.1, 128.4, 127.7, 126.41, 126.36, 122.3, 117.3, 115.8, 112.0, 59.0, 56.2, 56.1, 54.5 (2C), 53.9, 28.5, 27.8, 26.1, 25.5 (2C), 24.6, 24.2, 15.5; IR (neat) υ_{max}: 2934, 2213, 1584, 1503, 1321, 1253, 1231, 1136, 1022, 762 (cm^{-1}); HRMS (FAB): calcd for $C_{27}H_{38}N_3O_2S$ [M + H]$^+$, 468.2685; found, 468.2690.

***N*-(3,4-Dimethoxyphenyl)-6-ethyl-*N*-(2-(pyrrolidin-1-yl)ethyl)benzo[*d*]thiazol-2-amine (15).** (87.0 mg, 89%, yellow oil). ^{1}H NMR (400 MHz, CDCl$_3$): δ 7.29 (d, J = 8.0 Hz, 1H), 7.08 (dd, J = 8.3, 2.0 Hz, 1H), 7.00−6.96 (m, 2H), 6.89 (d, J = 8.3 Hz, 1H), 6.71−6.70 (m, 1H), 3.91 (s, 3H), 3.85 (s, 3H), 3.57 (t, J = 7.2 Hz, 2H), 2.82 (t, J = 7.2 Hz, 2H), 2.57−2.56 (m, 4H), 2.48 (q, J = 7.6 Hz, 2H), 1.80−1.77 (m, 4H), 1.09 (t, J = 7.6 Hz, 3H); ^{13}C NMR (100 MHz, CDCl$_3$): δ 150.0, 149.7, 145.2, 136.6, 135.0, 128.4, 127.7, 126.9, 126.4, 122.4, 117.3, 115.9, 112.0, 56.2, 56.1, 54.2 (2C), 53.4, 52.5, 28.5, 23.7 (2C) 15.5; IR (neat) υ_{max}: 2963, 2214, 1584, 1503, 1440, 1252, 1230, 1135, 1022, 806 (cm^{-1}); HRMS (ESI): calcd for $C_{23}H_{30}N_3O_2S$ [M + H]$^+$, 412.2053; found, 412.2048.

***N*-(3,4-Dimethoxyphenyl)-6-ethyl-*N*-(3-(pyrrolidin-1-yl)propyl)benzo[*d*]thiazol-2-amine (16).** (74.0 mg, 50%, yellow oil). ^{1}H NMR (400 MHz, CDCl$_3$): δ 7.22 (d, J = 8.0 Hz, 1H), 7.07 (dd, J = 8.3, 2.1 Hz, 1H), 6.99−6.96 (m, 2H), 6.88 (d, J = 8.3 Hz, 1H), 6.70−6.69 (m, 1H), 3.90 (s, 3H), 3.84 (s, 3H), 3.51 (t, J = 7.2 Hz, 2H), 2.68 (t, J = 7.3 Hz, 2H), 2.62−2.58 (m, 4H), 2.46 (q, J = 7.6 Hz, 2H), 2.06−1.99 (m, 2H), 1.82−1.78 (m, 4H), 1.07 (t, J = 7.6 Hz, 3H); ^{13}C NMR (100 MHz, CDCl$_3$): δ 150.0, 149.7, 145.2, 136.5, 135.0, 128.5, 127.7, 126.42, 126.35, 122.2, 117.2, 115.6, 112.0, 56.2, 56.1, 54.1 (2C), 53.1, 52.3, 28.5, 27.0, 23.5 (2C), 15.4; IR (neat) υ_{max}: 2985, 2214, 1585, 1503, 1442, 1253, 1231, 1137, 1023, 728 (cm^{-1}); HRMS (FAB): calcd for $C_{24}H_{32}N_3O_2S$ [M + H]$^+$, 426.2215; found, 426.2220.

***N*-(3,4-Dimethoxyphenyl)-6-ethyl-*N*-(4-(pyrrolidin-1-yl)butyl)benzo[*d*]thiazol-2-amine (17).** (101 mg, 74%, yellow oil). ^{1}H NMR (400 MHz, CDCl$_3$): δ 7.20 (d, J = 8.0 Hz, 1H), 7.07 (dd, J = 8.3, 2.1 Hz, 1H), 6.98−6.96 (m, 2H), 6.88 (d, J = 8.4 Hz, 1H), 6.69−6.68 (m, 1H), 3.90 (s, 3H), 3.84 (s, 3H), 3.44 (t, J = 6.9 Hz, 2H), 2.69−2.61 (m, 6H), 2.46 (q, J = 7.6 Hz, 2H), 1.87−1.74 (m, 8H), 1.07 (t, J = 7.6 Hz, 3H); ^{13}C NMR (100 MHz, CDCl$_3$): δ 150.0, 149.7, 145.3, 136.5, 135.0, 128.4, 127.7, 126.4, 126.3, 122.1, 117.2, 115.6, 112.0, 56.2, 56.1, 55.7, 54.1 (2C), 53.7, 28.5, 25.9, 25.1, 23.5 (2C), 15.4; IR (neat) υ_{max}: 2963, 2213, 1584, 1503, 1441, 1253, 1230, 1136, 1022, 728 (cm^{-1}); HRMS (ESI): calcd for $C_{25}H_{34}N_3O_2S$ [M + H]$^+$, 440.2366; found, 440.2364.

***N*-(3,4-Dimethoxyphenyl)-6-ethyl-*N*-(5-(pyrrolidin-1-yl)pentyl)benzo[*d*]thiazol-2-amine (18).** (87.0 mg, 60%, yellow oil). ^{1}H NMR (400 MHz, CDCl$_3$): δ 7.20 (d, J = 8.0 Hz, 1H), 7.08 (dd, J = 8.3, 2.0 Hz, 1H), 6.99−6.97 (m, 2H), 6.90 (d, J = 8.3 Hz, 1H), 6.70−6.69 (m, 1H), 3.91 (s, 3H), 3.85 (s, 3H), 3.43 (t, J = 7.3 Hz, 2H), 2.90−2.77 (m, 4H), 2.70 (t, J = 7.9 Hz, 2H), 2.47 (q, J = 7.6 Hz, 2H), 1.94−1.89 (m, 4H), 1.84−1.70 (m, 4H), 1.55−1.47 (m, 2H), 1.09 (t, J = 7.6 Hz, 3H); ^{13}C NMR (100 MHz, CDCl$_3$): δ 150.0, 149.8, 145.3, 136.6, 135.0, 128.4, 127.8, 126.44, 126.38, 122.2, 117.3, 115.7, 112.1, 56.3, 56.1, 55.9, 54.0 (2C), 53.7, 28.5, 27.6, 27.2, 24.3, 23.5 (2C), 15.5; IR (neat) υ_{max}: 2934, 2213, 1736, 1584, 1503, 1441, 1251, 1231, 1136, 1023, 806 (cm^{-1}); HRMS (FAB): calcd for $C_{26}H_{36}N_3O_2S$ [M + H]$^+$, 454.2528; found, 454.2520.

***N*-(3,4-Dimethoxyphenyl)-6-ethyl-*N*-(2-morpholinoethyl)benzo[*d*]thiazol-2-amine (19).** (18.0 mg, 84%, ivory solid). ^{1}H NMR (400 MHz, CDCl$_3$): δ 7.33 (d, J = 8.0 Hz, 1H), 7.09−7.07 (m, 1H), 7.00−6.97 (m, 2H), 6.90 (d, J = 8.3 Hz, 1H), 6.70−6.99 (m, 1H), 3.92 (s, 3H), 3.85 (s, 3H), 3.73−3.71 (m, 4H), 3.58 (t, J = 6.3 Hz, 2H), 2.67 (t, J = 6.1 Hz, 2H), 2.51−2.45 (m, 6H), 1.09 (t, J = 7.6 Hz, 3H); ^{13}C NMR (100 MHz, CDCl$_3$): δ 150.0, 149.8, 145.3, 136.5, 135.0, 128.4, 127.7, 127.0, 126.3, 122.2, 117.2, 115.9, 112.0, 66.9 (2C), 56.2, 56.1, 55.9, 53.6 (2C), 50.2, 28.5, 15.5; IR (neat) υ_{max}: 2934, 2214, 1584, 1503, 1440, 1252, 1230, 1115, 1022, 729 (cm^{-1}); HRMS (ESI): calcd for $C_{23}H_{30}N_3O_3S$ [M + H]$^+$, 428.2002; found, 428.1996.

***N*-(3,4-Dimethoxyphenyl)-6-ethyl-*N*-(3-morpholinopropyl)benzo[*d*]thiazol-2-amine (20).** (100 mg, 98%, yellow oil). ^{1}H NMR (400 MHz, CDCl$_3$): δ 7.22 (d, J = 8.0 Hz, 1H), 7.09−7.06 (m, 1H), 6.99−6.96 (m, 2H), 6.89 (d, J = 8.3 Hz, 1H), 6.71−6.70 (m, 1H), 3.90 (s, 3H), 3.84 (s, 3H), 3.68−3.66 (m, 4H), 3.51 (t, J = 7.2 Hz, 2H), 2.50−2.41 (m, 8H), 1.97−1.90 (m, 2H), 1.08 (t, J = 7.6 Hz, 3H); ^{13}C NMR (100 MHz, CDCl$_3$): δ 150.1, 149.8, 145.3, 136.6, 135.1, 128.4, 127.8, 126.4, 126.3, 122.2, 117.2, 115.7, 112.0, 66.9 (2C), 56.2, 56.1, 55.4, 53.6, 52.1, 29.8, 28.6, 24.8, 15.5; IR (neat) υ_{max}: 2935, 2213, 1584, 1503, 1441, 1252, 1230, 1115, 1022, 728 (cm^{-1}); HRMS (ESI): calcd for $C_{24}H_{32}N_3O_3S$ [M + H]$^+$, 442.2159; found, 442.2162.

***N*-(3,4-Dimethoxyphenyl)-6-ethyl-*N*-(4-morpholinobutyl)benzo[*d*]thiazol-2-amine (21).** (125 mg, 92%, white solid). ^{1}H NMR (400 MHz, CDCl$_3$): δ 7.21 (d, J = 8.0 Hz, 1H), 7.09−7.06 (m, 1H), 6.99−6.97 (m, 2H), 6.89 (d, J = 8.4 Hz, 1H), 6.70−6.69 (m, 1H), 3.91 (s, 3H), 3.84 (s, 3H), 3.71−3.68 (m, 4H), 3.45 (t, J = 7.3 Hz, 2H), 2.50−2.36 (m, 8H), 1.85−1.77 (m, 2H), 1.68−1.61 (m, 2H), 1.08 (t, J = 7.6 Hz, 3H); ^{13}C NMR (100 MHz, CDCl$_3$): δ 150.0, 149.8, 145.2, 136.6, 135.2, 128.4, 127.7, 126.4, 126.3, 122.2, 117.2, 115.7, 112.0, 67.0 (2C), 58.4, 56.2, 56.1, 53.9, 53.7 (2C), 28.5, 25.9, 23.4, 15.5; IR (neat) υ_{max}: 2934, 2213, 1677, 1584, 1503, 1253, 1231, 1116, 1022, 733 (cm^{-1}); HRMS (FAB): calcd for $C_{25}H_{34}N_3O_3S$ [M + H]$^+$, 456.2321; found, 456.2313.

***N*-(3,4-Dimethoxyphenyl)-6-ethyl-*N*-(5-morpholinopentyl)benzo[*d*]thiazol-2-amine (22).** (110 mg, 72%, yellow oil). ^{1}H NMR (400 MHz, CDCl$_3$): δ 7.21 (d, J = 8.0 Hz, 1H), 7.08 (dd, J = 8.3, 2.1 Hz, 1H), 6.99−6.96 (m, 2H), 6.89 (d, J = 8.4 Hz, 1H), 6.70−6.69 (m, 1H), 3.91 (s, 3H), 3.84 (s, 3H), 3.70−3.68 (m, 4H), 3.41 (t, J = 7.4 Hz, 2H), 2.50−2.41 (m, 6H), 2.33 (t, J = 7.4 Hz, 2H), 1.83−1.75 (m, 2H), 1.56−1.43 (m, 4H), 1.08 (t, J = 7.6 Hz, 3H); ^{13}C NMR (100 MHz, CDCl$_3$): δ 150.0, 149.7, 145.2, 136.6, 135.2, 128.4, 127.7, 126.4, 126.3, 122.2, 117.3, 115.7, 112.0, 67.0 (2C), 58.8, 56.2, 56.1, 53.9, 53.8 (2C), 28.5, 27.9, 26.2, 24.4, 15.5; IR (neat) υ_{max}: 2936, 2213, 1584, 1503, 1398, 1253, 1231, 1116, 1022, 731 (cm^{-1}); HRMS (ESI): calcd for $C_{26}H_{36}N_3O_3S$ [M + H]$^+$, 470.2472; found, 470.2464.

***N*^{1}-(3,4-Dimethoxyphenyl)-*N*^{2},*N*^{2}-diethyl-*N*^{1}-(6-ethylbenzo[*d*]thiazol-2-yl)ethane-1,2-diamine (23).** (68 mg, 69%, yellow oil). ^{1}H NMR (400 MHz, CDCl$_3$): δ 7.30 (d, J = 8.0 Hz, 1H), 7.09−7.06 (m, 1H), 6.99−6.97 (m, 2H), 6.89 (d, J = 8.3 Hz, 1H), 6.73−6.72 (m, 1H), 3.91 (s, 3H), 3.84 (s, 3H), 3.52 (t, J = 7.1 Hz, 2H), 2.79 (t, J = 7.1 Hz, 2H), 2.58 (q, J = 7.1 Hz, 4H), 2.48 (q, J = 7.6 Hz, 2H), 1.09 (t, J = 7.6 Hz, 3H), 1.02 (t, J = 7.1 Hz, 6H); ^{13}C NMR (100 MHz, CDCl$_3$): δ 149.9, 149.7, 145.1, 136.2, 135.4, 128.5, 127.6, 126.8, 126.4, 122.4, 117.1, 115.9, 112.0, 56.2, 56.1, 51.8, 50.8, 47.3 (2C), 28.5, 15.5, 11.7 (2C); IR (neat) υ_{max}: 2966, 2213, 1584, 1503, 1440, 1252, 1230, 1136, 1022, 729 (cm^{-1}); HRMS (ESI): calcd for $C_{23}H_{32}N_3O_2S$ [M + H]$^+$, 414.2210; found, 414.2204.

N^1-(3,4-Dimethoxyphenyl)-N^3,N^3-diethyl-N^1-(6-ethylbenzo[*d*]thiazol-2-yl)propane-1,3-diamine (24). (80.0 mg, 81%, yellow oil). ^{1}H NMR (400 MHz, $CDCl_3$): δ 7.22 (d, J = 8.0 Hz, 1H), 7.08 (dd, J = 8.3, 2.1 Hz, 1H), 7.00−6.97 (m, 2H), 6.89 (d, J = 8.3 Hz, 1H), 6.71−6.70 (m, 1H), 3.91 (s, 3H), 3.85 (s, 3H), 3.49 (t, J = 7.3 Hz, 2H), 2.59−2.44 (m, 8H), 1.96−1.88 (m, 2H), 1.09 (t, J = 7.6 Hz, 3H), 1.01 (t, J = 7.1 Hz, 6H); ^{13}C NMR (100 MHz, CDCl3): δ 150.0, 149.8, 145.3, 136.6, 135.1, 128.4, 127.8, 126.4, 126.3, 122.2, 117.3, 115.6, 112.0, 56.2, 56.1, 52.4, 49.8, 46.8 (2C), 29.8, 28.6, 25.3, 15.5, 11.3; IR (neat) υ_{max}: 2987, 2213, 1584, 1503, 1441, 1253, 1231, 1136, 1023, 806, 734 (cm^{-1}); HRMS (ESI): calcd for $C_{24}H_{34}N_3O_2S$ [M + H]$^+$, 428.2366; found, 428.2369.

N^1-(3,4-Dimethoxyphenyl)-N^4,N^4-diethyl-N^1-(6-ethylbenzo[*d*]thiazol-2-yl)butane-1,4-diamine (25). (108 mg, 82%, yellow oil). ^{1}H NMR (400 MHz, $CDCl_3$): δ 7.22 (d, J = 8.0 Hz, 1H), 7.08 (dd, J = 8.3, 2.1 Hz, 1H), 6.99−6.97 (m, 2H), 6.89 (d, J = 8.3 Hz, 1H), 6.70−6.69 (m, 1H), 3.91 (s, 3H), 3.85 (s, 3H), 3.45 (t, J = 7.4 Hz, 2H), 2.55 (q, J = 7.2 Hz, 4H), 2.51−2.44 (m, 4H), 1.82−1.74 (m, 2H), 1.65−1.58 (m, 2H), 1.08 (t, J = 7.6 Hz, 3H), 1.03 (t, J = 7.2 Hz, 6H); ^{13}C NMR (100 MHz, $CDCl_3$): δ 150.0, 149.8, 145.2, 136.6, 135.1, 128.4, 127.8, 126.42, 126.36, 122.3, 117.3, 115.7, 112.0, 56.2, 56.1, 54.0, 52.4, 46.9 (2C), 28.5, 26.1, 23.9, 15.5, 11.6 (2C); IR (neat) υ_{max}: 2966, 2213, 1584, 1503, 1441, 1398, 1253, 1231, 1138, 1023, 762 (cm^{-1}); HRMS (ESI): calcd for $C_{25}H_{36}N_3O_2S$ [M + H]$^+$, 442.2523; found, 442.2519.

N^1-(3,4-Dimethoxyphenyl)-N^5,N^5-diethyl-N^1-(6-ethylbenzo[*d*]thiazol-2-yl)pentane-1,5-diamine (26). (119 mg, 80%, yellow oil). ^{1}H NMR (400 MHz, $CDCl_3$): δ 7.22 (d, J = 8.0 Hz, 1H), 7.09 (dd, J = 8.3, 2.1 Hz, 1H), 7.00−6.97 (m, 2H), 6.90 (d, J = 8.3 Hz, 1H), 6.71 (d, J = 2.0 Hz, 1H), 3.92 (s, 3H), 3.86 (s, 3H), 3.43 (t, J = 7.4 Hz, 2H), 2.62−2.57 (m, 4H), 2.51−2.45 (m, 4H), 1.85−1.77 (m, 2H), 1.60−1.52 (m, 2H), 1.49−1.41 (m, 2H), 1.11−1.04 (m, 9H); ^{13}C NMR (100 MHz, $CDCl_3$): δ 150.0, 149.8, 145.3, 136.6, 135.1, 128.3, 127.8, 126.4 (2C), 122.2, 117.3, 115.7, 112.1, 56.2, 56.1, 53.8, 52.4, 46.8 (2C), 28.5, 27.8, 25.7, 24.4, 15.5, 10.7 (2C); IR (neat) υ_{max}: 2967, 2213, 1738, 1584, 1503, 1253, 1231, 1137, 1023, 762 (cm^{-1}); HRMS (ESI): calcd for $C_{26}H_{38}N_3O_2S$ [M + H]$^+$, 456.2679; found, 456.2675.

N^1-Cyclohexyl-N^2-(3,4-dimethoxyphenyl)-N^2-(6-ethylbenzo[*d*]thiazol-2-yl)ethane-1,2-diamine (27). (99.0 mg, 95%, ivory solid). ^{1}H NMR (400 MHz, $CDCl_3$): δ 7.11 (d, J = 8.0 Hz, 1H), 7.07−7.04 (m, 1H), 6.99−6.96 (m, 2H), 6.86 (d, J = 8.3 Hz, 1H), 6.68−6.67 (m, 1H), 4.10−3.95 (m, 3H), 3.88 (s, 3H), 3.82 (s, 3H), 3.70−3.69 (m, 2H), 3.45 (t, J = 7.7 Hz, 2H), 2.46 (q, J = 7.6 Hz, 2H), 1.89−1.87 (m, 2H), 1.79−1.76 (m, 2H), 1.66−1.63 (m, 1H), 1.52−1.30 (m, 4H), 1.08 (t, J = 7.6 Hz, 3H); ^{13}C NMR (100 MHz, $CDCl_3$): δ 158.5, 149.9, 149.6, 145.4, 139.7, 133.2, 128.3, 127.9, 127.4, 126.4, 122.1, 117.4, 111.9, 56.2, 56.0, 53.1 (2C), 47.4, 40.6, 29.8, 28.6, 25.7, 25.4 (2C), 15.4; IR (neat) υ_{max}: 3315, 2931, 1655, 1549, 1503, 1253, 1230, 1136, 1020, 729 (cm^{-1}); HRMS (ESI): calcd for $C_{25}H_{34}N_3O_2S$ [M + H]$^+$, 440.2366; found, 440.2362.

N^1-Cyclohexyl-N^3-(3,4-dimethoxyphenyl)-N^3-(6-ethylbenzo[*d*]thiazol-2-yl)propane-1,3-diamine (28). (83 mg, 54%, ivory solid). ^{1}H NMR (400 MHz, $CDCl_3$): δ 7.12−7.09 (m, 2H), 7.03−7.00 (m, 2H), 6.94 (d, J = 8.4 Hz, 1H), 6.60−6.59 (m, 1H), 4.52 (tt, J = 11.6, 3.5 Hz, 1H), 3.93 (s, 3H), 3.88 (s, 3H), 3.68−3.62 (m, 1H), 3.55−3.41 (m, 3H), 2.48 (q, J = 7.6 Hz, 2H), 2.28−2.14 (m, 2H), 1.96−1.69 (m, 8H), 1.54−1.43 (m, 2H), 1.10 (t, J = 7.5 Hz, 3H); ^{13}C NMR (100 MHz, $CDCl_3$): δ 152.4, 150.7, 150.0, 147.7, 139.5, 132.1, 129.1, 128.6, 127.3, 126.9, 119.2, 118.1, 112.3, 58.1, 56.5, 56.1, 48.0, 39.7, 30.14, 30.09, 28.8, 25.4, 24.9, 24.8, 21.8, 15.4; IR (neat) υ_{max}: 3453, 2932, 1583, 1503, 1321, 1253, 1231, 1137, 1020, 725 (cm^{-1}); HRMS (ESI): calcd for $C_{26}H_{36}N_3O_2S$ [M + H]$^+$, 454.2523; found, 454.2517.

N^1-Cyclohexyl-N^4-(3,4-dimethoxyphenyl)-N^4-(6-ethylbenzo[*d*]thiazol-2-yl)butane-1,4-diamine (29). (91.0 mg, 58%, white solid). ^{1}H NMR (400 MHz, $CDCl_3$): δ 7.21 (d, J = 8.0 Hz, 1H), 7.08 (dd, J = 8.3, 2.0 Hz, 1H), 6.99−6.96 (m, 2H), 6.89 (d, J = 8.3 Hz, 1H), 6.70−6.69 (m, 1H), 3.91 (s, 3H), 3.84 (s, 3H), 3.43 (t, J = 7.4 Hz, 2H), 2.69 (t, J = 7.3 Hz, 2H), 2.50−2.44 (m, 3H), 1.90−1.57 (m, 10H), 1.28−1.05 (m, 8H); ^{13}C NMR (100 MHz, $CDCl_3$): δ 150.0, 149.7, 145.2, 136.6, 135.1, 128.3, 127.8, 126.41, 126.35, 122.2, 117.3, 115.7, 112.0, 57.0, 56.2, 56.0, 53.9 (2C), 46.2, 33.1, 28.5, 26.9, 26.1, 25.9, 25.1 (2C), 15.5; IR (neat) υ_{max}: 2929, 2213, 1585, 1503, 1442, 1253, 1230, 1136, 1023, 728 (cm^{-1}); HRMS (ESI): calcd for $C_{27}H_{38}N_3O_2S$ [M + H]$^+$, 468.2679; found, 468.2675.

N^1-Cyclohexyl-N^5-(3,4-dimethoxyphenyl)-N^5-(6-ethylbenzo[*d*]thiazol-2-yl)pentane-1,5-diamine (30). (112 mg, 72%, yellow oil). ^{1}H NMR (400 MHz, $CDCl_3$): δ 7.19 (d, J = 8.0 Hz, 1H), 7.07 (dd, J = 8.3, 2.1 Hz, 1H), 6.99−6.95 (m, 2H), 6.88 (d, J = 8.3 Hz, 1H), 6.69−6.68 (m, 1H), 3.90 (s, 3H), 3.84 (s, 3H), 3.41 (t, J = 7.4 Hz, 2H), 2.69 (t, J = 7.5 Hz, 2H), 2.53−2.43 (m, 3H), 1.94−1.90 (m, 2H), 1.82−1.70 (m, 4H), 1.66−1.58 (m, 3H), 1.51−1.45 (m, 2H), 1.25−1.11 (m, 5H), 1.07 (t, J = 7.6 Hz, 3H); ^{13}C NMR (100 MHz, $CDCl_3$): δ 150.0, 149.7, 145.2, 136.6, 135.1, 128.3, 127.8, 126.4, 126.3, 122.2, 117.3, 115.7, 112.0, 57.0, 56.2, 56.1, 53.9 (2C), 46.1, 32.6, 29.0, 28.5, 27.8, 25.9, 25.0 (2C), 24.3, 15.4; IR (neat) υ_{max}: 2929, 2213, 1584, 1503, 1321, 1253, 1231, 1023, 729 (cm^{-1}); HRMS (ESI): calcd for $C_{28}H_{40}N_3O_2S$ [M + H]$^+$, 482.2836; found, 482.2833.

N^1-Cyclopentyl-N^2-(3,4-dimethoxyphenyl)-N^2-(6-ethylbenzo[*d*]thiazol-2-yl)ethane-1,2-diamine (31). (767 mg, 76%, white solid). ^{1}H NMR (400 MHz, CD_2Cl_2): δ 7.13 (d, J = 8.0 Hz, 1H), 7.09 (dd, J = 8.3, 2.1 Hz, 1H), 7.02−7.00 (m, 2H), 6.90 (d, J = 8.3 Hz, 1H), 6.75−6.74 (m, 1H), 4.38−4.31 (m, 1H), 3.86 (s, 3H), 3.79 (s, 3H), 3.72−3.61 (m, 3H), 3.36 (t, J = 7.2 Hz, 2H), 2.49 (q, J = 7.6 Hz, 2H), 1.90−1.84 (m, 2H), 1.74−1.54 (m, 6H), 1.10 (t, J = 7.6 Hz, 3H); ^{13}C NMR (100 MHz, $CDCl_3$): δ 150.0, 149.7, 145.1, 136.4, 135.2, 128.4, 127.6, 127.1, 126.3, 122.5, 117.2, 116.0, 112.0, 56.24, 56.21, 56.1, 54.7 (2C), 51.0, 28.5, 26.0 (2C), 24.4, 15.5; IR (neat) υ_{max}: 3173, 2961, 1658, 1547, 1498, 1253, 1228, 1136, 1019, 804 (cm^{-1}); HRMS (FAB): calcd for $C_{24}H_{32}N_3O_2S$ [M + H]$^+$, 426.2215; found, 426.2214.

N^1-Cyclopentyl-N^3-(3,4-dimethoxyphenyl)-N^3-(6-ethylbenzo[*d*]thiazol-2-yl)propane-1,3-diamine (32). (91.0 mg, 61%, ivory solid). ^{1}H NMR (400 MHz, $CDCl_3$): δ 7.13−7.08 (m, 2H), 7.02−6.99 (m, 2H), 6.94 (d, J = 8.4 Hz, 1H), 6.60−6.59 (m, 1H), 5.02−4.94 (m, 1H), 3.93 (s, 3H), 3.88 (s, 3H), 3.70−3.64 (m, 1H), 3.54−3.48 (m, 1H), 3.43 (t, J = 5.8 Hz, 2H), 2.48 (q, J = 7.6 Hz, 2H), 2.32−2.13 (m, 4H), 1.86−1.50 (m, 7H), 1.09 (t, J = 7.6 Hz, 3H); ^{13}C NMR (100 MHz, $CDCl_3$): δ 152.9, 150.7, 150.0, 147.7, 139.6, 132.2, 129.1, 128.6, 127.2, 126.8, 119.3, 118.1, 112.3, 60.0, 56.4, 56.1, 47.9, 40.0, 29.2, 28.8, 28.7, 24.3, 24.2, 21.9, 15.4; IR (neat) υ_{max}: 3320, 2921, 1639, 1583, 1503, 1442, 1253, 1231, 1021, 729 (cm^{-1}); HRMS (ESI): calcd for $C_{25}H_{34}N_3O_2S$ [M + H]$^+$, 440.2366; found, 440.2373.

N^1-Cyclopentyl-N^4-(3,4-dimethoxyphenyl)-N^4-(6-ethylbenzo[*d*]thiazol-2-yl)butane-1,4-diamine (33). (140 mg, 37%, colorless oil). ^{1}H NMR (400 MHz, $CDCl_3$): δ 7.20 (d, J = 8.0 Hz, 1H), 7.06 (dd, J = 8.3, 2.1 Hz, 1H), 6.99−6.95 (m, 2H), 6.88 (d, J = 8.3 Hz, 1H), 6.67−6.66 (m, 1H), 3.90 (s, 3H), 3.83 (s, 3H), 3.43 (t, J = 7.3 Hz, 2H), 3.38−3.31 (m, 1H), 2.92 (t, J = 8.0 Hz, 2H), 2.45 (q, J = 7.6 Hz, 2H), 2.05−1.97 (m, 4H), 1.92 (s, 1H), 1.87−1.79 (m, 6H), 1.58−1.49 (m, 2H), 1.06 (t, J = 7.6 Hz, 3H); ^{13}C NMR (100 MHz, $CDCl_3$): δ 150.1, 149.8, 145.5, 136.7, 134.6, 128.3, 127.9, 126.54, 126.49, 121.9, 117.3, 115.5, 112.1, 59.3, 56.3, 56.1, 53.2, 46.4, 29.8 (2C), 28.5, 25.5, 23.9 (2C), 23.0, 15.5; IR (neat) υ_{max}: 3401, 2958, 2212, 1583, 1502, 1440, 1252, 1230, 1135, 1021, 762 (cm^{-1}); HRMS (FAB): calcd for $C_{26}H_{36}N_3O_2S$ [M + H]$^+$, 454.2528; found, 454.2527.

N^1-Cyclopentyl-N^5-(3,4-dimethoxyphenyl)-N^5-(6-ethylbenzo[*d*]thiazol-2-yl)pentane-1,5-diamine (34). (136 mg, 89%, yellow oil). ^{1}H NMR (400 MHz, $CDCl_3$): δ 7.20 (d, J = 8.0 Hz, 1H), 7.09−7.06 (m, 1H), 6.99−6.96 (m, 2H), 6.89 (d, J = 8.3 Hz, 1H), 6.69−6.68 (m, 1H), 3.90 (s, 3H), 3.84 (s, 3H), 3.41 (t, J = 7.4 Hz, 2H), 3.10−3.03 (m, 1H), 2.61 (t, J = 7.2 Hz, 2H), 2.47 (q, J = 7.6 Hz, 2H), 1.90−1.74 (m, 4H), 1.72−1.62 (m, 2H), 1.61−1.43 (m, 6H), 1.39−1.31 (m, 2H), 1.08 (t, J = 7.6 Hz, 3H); ^{13}C NMR (100 MHz, $CDCl_3$): δ 149.9, 149.7, 145.1, 136.6, 135.1, 128.3, 127.7, 126.33, 126.27 122.2, 117.2, 115.7, 112.0, 59.9, 56.1, 56.0, 53.9, 48.3, 32.8 (2C), 29.5, 28.4, 27.8, 24.3, 24.1 (2C), 15.4; IR (neat) υ_{max}: 2937, 2213, 1585, 1503, 1321, 1253, 1231, 1023, 728 (cm^{-1}); HRMS (ESI): calcd for $C_{27}H_{38}N_3O_2S$ [M + H]$^+$, 468.2679; found, 468.2697.

6-Ethyl-*N*-(3-methoxyphenyl)-*N*-(3-(piperidin-1-yl)propyl)-benzo[*d*]thiazol-2-amine (12). To a solution of **53** (200 mg, 0.49 mmol) in DMF/MeCN (1:1, 5 mL, 0.1 M) was added K_2CO_3 (273 mg, 1.97 mmol) and piperidine (484 μL, 4.90 mmol). The reaction mixture was stirred at 50 °C for 14 h and then diluted with H_2O and extracted with EtOAc. The organic layer was dried over $MgSO_4$, filtered, and evaporated *in vacuo*. The crude product was separated by silica gel column chromatography (CH_2Cl_2/MeOH, 20:1, R_f = 0.2) to produce the desired product **12** (84.0 mg, 42%, colorless oil). ^{1}H NMR (400 MHz, $CDCl_3$): δ 7.28 (d, *J* = 8.0 Hz, 1H), 7.26−7.22 (m, 1H), 7.09 (dd, *J* = 8.0, 2.0 Hz, 1H), 7.04−7.03 (m, 1H), 6.92−6.89 (m, 1H), 6.89−6.88 (m, 1H), 6.83 (ddd, *J* = 8.2, 2.5, 0.7 Hz, 1H), 3.77 (s, 3H), 3.46 (t, *J* = 7.3 Hz, 2H), 2.54 (q, *J* = 7.6 Hz, 2H), 2.38−2.32 (m, 6H), 1.88 (td, *J* = 14.6, 7.3 Hz, 2H), 1.57−1.51 (m, 4H), 1.43−1.39 (m, 2H) 1.14 (t, *J* = 7.6 Hz, 3H); ^{13}C NMR (100 MHz, $CDCl_3$): δ 160.3, 145.1, 137.5, 135.2, 133.0, 132.2, 130.3, 128.1, 126.4, 123.8, 116.6, 115.6, 113.8, 55.7, 55.5, 54.5 (2C), 52.5, 28.4, 25.9 (2C), 25.2, 24.4, 15.4; IR (neat) υ_{max}: 2933, 2772, 2213, 1589, 1480, 1426, 1230, 1038, 857, 774, 687 (cm^{-1}); HRMS (FAB): calcd for $C_{24}H_{32}N_3OS$ [M + H]$^+$, 410.2266; found, 410.2260.

All **13** and **14** compounds were synthesized using a similar procedure to that for compound **12**.

***N*-(3,4-Difluorophenyl)-6-ethyl-*N*-(3-(piperidin-1-yl)propyl)-benzo[*d*]thiazol-2-amine (13).** (30.0 mg, 56%, white solid). ^{1}H NMR (400 MHz, $CDCl_3$): δ 7.29 (d, *J* = 8.1 Hz, 1H), 7.18−7.07 (m, 4H), 7.00−6.99 (m, 1H), 3.46 (t, *J* = 7.6 Hz, 2H), 2.56 (q, *J* = 7.6 Hz, 2H), 2.38−2.32 (m, 6H), 1.88 (td, *J* = 14.5, 7.2 Hz, 2H), 1.56−1.50 (m, 4H), 1.43−1.39 (m, 2H), 1.15 (t, *J* = 7.6 Hz, 3H); ^{13}C NMR (100 MHz, $CDCl_3$): δ 151.70 (dd, *J* = 12.9, 45.7 Hz, 1C), 149.20 (dd, *J* = 12.7, 44.1 Hz, 1C), 145.3, 137.7, 132.4, 132.1, 130.52 (t, *J* = 5.0 Hz, 1C), 128.6, 128.04 (q, *J* = 3.3 Hz, 1C), 126.5, 120.65 (d, *J* = 18.2 Hz, 1C), 118.34 (d, *J* = 17.7 Hz, 1C), 115.4, 55.7, 54.6 (2C), 52.6, 28.4, 26.1 (2C), 25.3, 24.5, 15.4; IR (neat) υ_{max}: 2934, 2214, 1600, 1501, 1486, 1403, 1272, 1200, 1116, 903, 771 (cm^{-1}); HRMS (FAB): calcd for $C_{23}H_{28}F_2N_3S$ [M + H]$^+$, 416.1972; found, 416.1964.

6-Ethyl-*N*-(3-(piperidin-1-yl)propyl)-*N*-(4-(trifluoromethyl)-phenyl)benzo[*d*]thiazol-2-amine (14). (45.0 mg, 56%, yellow oil). ^{1}H NMR (400 MHz, $CDCl_3$): δ 7.49 (d, *J* = 8.3 Hz, 2H), 7.34−7.31 (m, 1H), 7.26−7.23 (m, 2H), 7.20−7.19 (m, 2H), 3.43 (t, *J* = 7.3 Hz, 2H), 2.57 (q, *J* = 7.6 Hz, 2H), 2.31−2.28 (m, 6H), 1.81 (td, *J* = 14.4, 7.2 Hz, 2H), 1.52−1.46 (m, 4H), 1.38−1.37 (m, 2H), 1.16 (t, *J* = 7.6 Hz, 3H); ^{13}C NMR (100 MHz, $CDCl_3$): δ 145.4, 141.0, 139.5, 134.9, 129.8, 129.6, 129.0 (2C), 128.83 (q, *J* = 32.4 Hz, 1C), 126.5, 126.19 (q, *J* = 3.7 Hz, 2C), 124.1 (q, *J* = 269.6 Hz, 1C), 115.3, 55.6, 54.6 (2C), 52.7, 28.3, 26.0 (2C), 25.2, 24.4, 15.4; IR (neat) υ_{max}: 2935, 2214, 1605, 1486, 1323, 1163, 1122, 1089, 1062, 1013, 827 (cm^{-1}); HRMS (FAB): calcd for $C_{24}H_{29}F_3N_3S$ [M + H]$^+$, 448.2034; found, 448.2024.

Chemicals and Reagents. 3-(4,5-Dimethylthiazol-2-yl)-2,5-diphenyltetrazolium bromide (MTT), DMSO, and gelatin were purchased from Sigma-Aldrich (St. Louis, MO, USA). All the tested compounds were dissolved in 100% DMSO, and the final concentration of DMSO was 0.1% for all the *in vitro* experiments. Recombinant human VEGF ($VEGF_{165}$) was obtained from PeproTech (Rocky Hill, NJ, USA). Growth factor-reduced Matrigel was purchased from BD Biosciences (San Jose, CA, USA). Antibodies against IL-1*β* (sc-32294), NF*κ*B p50 (sc-8414), NF*κ*B p65 (sc-372), and *β*-actin (sc-47778) were obtained from Santa Cruz Biotechnology (Santa Cruz, CA, USA). *p*-VEGFR2 (#2478), VEGFR2 (#2479), p-PI3K (#4228), PI3K (#4249), c-Abl (#2862), and STAT5 (#25656) were purchased from Cell Signaling Technology (Danvers, MA, USA). p-STAT5 (#71-6900) was purchased from Invitrogen (Invitrogen, Carlsbad, CA, USA). ANGPT2 (24613-1-AP) was purchased from Proteintech (Rosemont, IL, USA). Secondary antibodies were purchased from Younginfrontier (Seoul, Korea).

Cell Culture. HUVEC and ARPE-19 cells were obtained from the ATCC (Rockville, MD, USA). HRMECs were obtained from Cell Systems (Kirkland, MA, USA). HUVECs and HRMECs were cultured using EGM-2 Bulletkit (Lonza, Walkersville, MD, USA) supplemented with 10% FBS and 1% antibiotics-antimycotics (AA) (PSF; 100 units/mL of penicillin G sodium, 100 μg/mL of streptomycin, and 250 ng/mL of amphotericin B), and ARPE-19 cells were cultured in Dulbecco's modified Eagle's medium/nutrient mixture F-12 (DMEM/F-12) (Gibco, Grand Island, NY, USA) supplemented with 10% FBS and 1% AA. All the cells were maintained at 37 °C in a 5% CO_2 atmosphere.

Tube Formation and Cell Viability Test. HUVECs or HRMECs (1.5 × 10^4 cells/well) were mixed with various compound concentrations and seeded onto each well of a Matrigel-coated 96-well plate. The cells were then incubated for 6 h at 37 °C in a 5% CO_2 atmosphere and photographed using an inverted microscope. In our previous study, the number of branches for each image was counted by the eye. To obtain more accurate data, we modified the method to calculate the total segment lengths per image using the angiogenesis analyzer for ImageJ. Consequently, the IC_{50} values of the previous and present studies are not directly comparable. The following formula was used for quantification: 100 × (avg. of tot. seg.$_{\text{length compound}}$ − avg. of tot. seg.$_{\text{length VEGF(−)control}}$)/(avg. of tot. seg.$_{\text{length VEGF(+)control}}$ − avg. of tot. seg.$_{\text{length VEGF(−)control}}$). For cell viability, HUVECs were seeded in 96-well plates (8 × 10^3 cells/well). On the next day, the cells were serum-starved overnight and treated with various concentrations of compounds in EBM-2 media with 2% FBS for 24 h in the presence of VEGF (50 ng/mL). Cell viability was assayed by the MTT method. The IC_{50} values were calculated via log (inhibitor) versus normalized response (variable slope) analysis using GraphPad Prism (GraphPad Software, San Diego, CA).

VEGFR-2 Tyrosine Kinase Assay. VEGFR-2 tyrosine kinase activities of the compounds were measured with the VEGFR-2 tyrosine kinase assay kit (BPS Bioscience, San Diego, CA, USA) and the Kinase-Glo MAX luminescence kinase assay kit (Promega, Madison, WI, USA). The kinase assay kits determine kinase activity with the inhibitor by quantitating the number of ATP molecules in the solution. Kinase activity of the reaction lowers the amount of ATP remaining in the solution; therefore, the luminescence intensity is conversely correlated with the kinase activity. The compounds were dissolved in 10% DMSO in the assay to make 1% DMSO concentration in every reaction mixtures. The final reaction mixture was made of 10 mM $MgCl_2$, 10 μM ATP, 40 mM Tris (pH 7.4), 0.1 mg/mL BSA, kinase substrate, and the enzyme. All of the enzymatic reactions were incubated at 30 °C for 45 min. After the incubating time, 50 μL of Kinase-Glo Max luminescence solution (Promega, Madison, WI, USA) was added to each well. The plate was covered with aluminum foil and incubated at room temperature for 15 min. Luminescence intensity of each well was determined using a Centro LB 960 microplate luminometer. Inhibition activity was calculated using the following equation: 100 − [100 × (test compound signal − blank signal)/(negative control signal − blank signal)].

Migration Assay. HUVECs were seeded onto six-well plates in full media. When the cells were fully grown, they were scratched with a 10 μL tip. The media were removed and replaced with 2% FBS/EGM-2 and treated with DMSO or the indicated concentrations of the test compound. After 24 h, the cells were visualized and photographed using an inverted microscope.

High Glucose-Induced Model. Cells were seeded onto 60 mm dishes. When the cells reached 80% confluency, the media were removed and replaced with media supplemented with 2% FBS. The cells were treated with DMSO or the indicated concentrations of the test compound for 30 min, and a final concentration of 5.5 mM or 30 mM D-glucose was added to the media. The cells were further incubated for 48 h at 37 °C in a 5% CO_2 atmosphere.

Western Blotting Analysis. The cells were lysed in 2× sample loading buffer (250 mM Tris−HCl (pH 6.8), 4% SDS, 10% glycerol, 0.006% bromophenol blue, 2% *β*-mercaptoethanol, 50 mM sodium fluoride, and 5 mM sodium orthovanadate). The collected samples were subjected to 6−12% SDS-PAGE and transferred to PVDF membranes (Millipore, Bedford, MA, USA). The membranes were blocked with 5% BSA in Tris-buffered saline containing 0.1% Tween-20 (TBST) for 1 h at room temperature and then incubated with primary antibodies in 2.5% BSA in TBST overnight at 4 °C on a shaker. The membranes were washed three times with TBST and incubated with secondary antibodies (HRP) (Younginfrontier, Seoul, Korea) diluted in TBST for 2 h at room temperature. After washing with TBST, the membranes were exposed to enhanced chemiluminescence solution (Intron, Daejeon, Korea). The chemiluminescence signals were captured using the LAS-4000 system (Fuji Film Corp., Tokyo, Japan).

Real-Time PCR Analysis. The total RNA of the cells was isolated using NucleoZOL (Macherey-Nagel GmbH & Co., KG, Duren, Germany). The isolated RNA (1 μg) was reverse transcribed using ReverTra Ace qPCR RT Master Mix (TOYOBO, Osaka, Japan) according to the manufacturer's instructions. Using synthesized cDNA, real-time PCR was conducted using iQTM SYBR Green Supermix (Bio-Rad, Hercules, CA, USA) according to the manufacturer's instructions. The sequences of the primers used were *ANGPT2* (F) 5′-ATTCAGCGACGTGAGGATGGCA-3′ (R) 5′-GCACATAGCGTTGCTGATTAGTC-3′ and *HPRT1* (F) 5′-TGCAGACTTTGCTTTCCTTGGTCAGG-3′ (R) 5′-CCAA-CACTTCGTGGGGTCCTTTTCA-3′

Laser-Induced CNV in Mice. C57BL/6 mice (Orientbio Inc, Korea) were treated in accordance with the Guide of the Care and Use of Laboratory Animals and Association for Research in Vision and Ophthalmology Statement for the Use of Animals in Ophthalmic and Vision Research and approved by the Institutional Animal Care and Use Committee at KPC Labs. For the induction of CNV, mice were anesthetized by the ketamine (ketamine 100 mg + xylazine 10 mg/10 mL/kg). Anesthesia one eye drops (0.5% proparacaine) were applied to pupils for further local anesthesia. The laser (Meridian Merilas 532 green laser photocoagulator) burn induced according to the CNV induction condition (wavelength 532 nm, diameter 50 μm, duration 80 mS, and power level 200 mW) to break the Bruch's membrane. One drop of antibiotic mucus (0.3% tobramycin) was applied to the eye with the CNV induction completed. Mice were administered with drugs 1 day after CNV induction for 11 days. Eylea was injected into the scleral puncture with a 34G needle connected to the IO kit and then administered to both eyes (3 mg/mL concentration, 1 μL/eye) once a day. Vehicle and 1% **31** eye drops were applied to mouse eyes (1 μL/eye) four times a day. When the administration was completed, an antibiotic ophthalmic solution was instilled in the eye of the mouse to prevent infection.

Fundus Fluorescent Angiography/Optical Coherence Tomography Angiography. On the 10th day after CNV induction, mice were anesthetized with ketamine, and then, a fluorescent contrast agent (10% fluorescite 1 mL/kg) was injected intraperitoneally. Anesthesia eye drops were instilled into the eye, followed by additional local anesthesia. The mouse was placed on the sacrifice table, and the image was adjusted to the fundus with the Micron-IV imaging camera (Phoenix, CA, USA), and the lubricating gel was instilled on the eye. The lens of the OCTA was brought into contact with the cornea of the mouse. After FFA/OCTA imaging was performed, a drop of antibiotic ophthalmic solution was instilled on the mouse eye. FFA and OCTA images were analyzed using the ImageJ program (National Institutes of health, Bethesda, MD).

ERG Recording. Each mouse was subjected to induced dark adaptation in the dark from 12 h before ERG evaluation. On the day of evaluation (11 days after CNV induction), after general anesthesia with rompun and ketamine, an alkaline solution was instilled into the eye to induce additional local anesthesia. The mouse was placed on an ERG staging table, and the ERG probe was made to contact the tail, head, and cornea. ERG was measured as the change in the retinal potential for a single flash stimulation [0.9 log cds/m^2 (10 responses/intensity)]. When the ERG evaluation was completed, a drop of Tobrex was instilled into the mouse eye. ERG analysis was performed using the Lab Scribe ERG program (iWorx Data Acquisition Software).

Mouse Model of OIR. The animals were cared for in accordance with the Guide for the Care and Use of Laboratory Animals published by the United States National Institutes of Health. The protocols were also approved by the Institutional Animal Care and Use Committee of Chung-Ang University. Pregnant C57BL/6 mice were purchased from Orientbio Inc. (Seoul, Korea). The mice were housed in microisolator cages on individually ventilated cage racks with access to an autoclaved standard rodent diet ad libitum (LabDiet 5008, Purina, St. Louis, MO, USA) and were kept under a 12:12 h light−dark cycle. For the surgical procedures, the mice were anesthetized with an intraperitoneal injection of ketamine hydrochloride (100 mg/kg of body weight) and xylazine hydrochloride (6 mg/kg of body weight). The pupils of the anesthetized mice were dilated with topical drops of 1% tropicamide (Santen, Osaka, Japan). The litters of newborn mice and their nursing mothers were placed in a hyperoxic (75% oxygen) chamber connected to an oxygen controller (ProOx P110; BioSpherix, Parish, NY, USA) from postnatal day (P)7 to P12 (Phase I: vaso-obliteration). At P12, the mice were returned to room air with a normal oxygen content and received a single intravitreal injection of **31** (3 μg/μL in DMSO) or an equivalent volume of DMSO. Uninjected contralateral eyes were served as controls. At P17, after 5 days of exposure to room air, the mice were sacrificed, and both eyes were harvested for the analysis of the retinal vasculature (Phase II; neovascularization). Underdeveloped neonatal mice with weights less than 6 g at P17 were excluded. In Phase I, hyperoxia inhibits central vessel growth in the retina and causes significant vessel regression; in Phase II, hypoxia enhances the expression of angiogenic factors, such as VEGF, triggering pathological neovascularization, which reaches a maximum at P17.

Quantification of Retinal Neovascularization. The eyes were enucleated and fixed overnight in 4% paraformaldehyde. The retinas were then dissected and stained overnight at 4 °C with Alexa Fluor 594-conjugated Griffonia Bandeiraea Simplicifolia isolectin B4 (IB4, 1:100 dilution; Invitrogen, Carlsbad, CA, USA). The retinas were rinsed three times with PBS, flat-mounted on microscope slides, and imaged using a fluorescence microscope (Olympus, Tokyo, Japan); the exposure and gain were kept constant for all samples. In each image, the number of pixels of preretinal neovascular tufts was determined using ImageJ software (National Institutes of Health, Bethesda, MD, USA) and compared with the total number of pixels in the entire retinal area.

Solubility Analysis. The solubility of compound **31** was measured using the pH-metric CheqSol technique[38,39] (Sirius Analytical Instruments Ltd.). Experiments were performed in 0.15 M KCl solution under a nitrogen atmosphere at 25 °C and titrated using standardized 0.5 M HCl and 0.5 M KOH solutions.

KINOMEscan. The kinase profile of **31** was evaluated using DiscoverX KINOMEscan as previously described.[40] Binding affinity of compound **31** at 10 μM was evaluated against 468 kinase panels. The binding interactions were calculated using the following equation. % Ctrl calculation = 100 × (test compound signal − positive control signal)/(negative control signal − positive control signal), where negative control is DMSO and positive control is the control compound.

Metabolic Stability. To the mix buffer [0.1 M phosphate buffer (182 μL, pH 7.4)] was added NADPH-regenerating system solution A followed by NADPH-regenerating system solution B. A stock solution of **31** (1 μL, 200 μM) was added, and the mixture was prewarmed to 37 °C for 10 min. Pooled liver microsomes (5 μL, prewarmed in a 37 °C water bath before use) were added. At selected time points (0 and 30 min), aliquots (30 μL) were withdrawn from the tube, and cold acetonitrile (120 μL) containing an internal standard (chlorpromazine) was added to stop the reaction. The samples were centrifuged at 14,000 rpm for 10 min at 4 °C. The supernatant (30 μL) was withdrawn and transferred to a sample vial containing an insert. LC−MS/MS analysis was performed using an Agilent 1290 infinity II and AB SCIEX Triple Quad 6500 plus system. Chromatographic separation was performed by injecting 5 μL of the sample onto a Phenomenex Luna C18 column (2 × 50 mm, 3 μm). The flow conditions were 50% solvent A (water containing 0.1%

formic acid) and 50% solvent B (acetonitrile containing 0.1% formic acid). The flow rate was 0.3 mL/min.

Plasma Stability. The buffered plasma was prepared by mixing 0.1 M PBS and plasma in a ratio of 1:9. Buffed plasma (195 μL) was prewarmed to 37 °C for 10 min, and stock solution of **31** (5 μL, 40 μM) was added. At selected time points (0, 120 min), aliquots (30 μL) were withdrawn from the tube and cold acetonitrile (120 μL) containing an internal standard (chlorpromazine) was added to stop reaction. The samples were centrifuged at 14,000 rpm for 10 min at 4 °C. The supernatant (30 μL) was withdrawn and transferred to a sample vial with the insert. LC−MS/MS analysis was performed on an Agilent 1290 infinity II and AB SCIEX Triple Quad 6500 plus system. Chromatographic separation was performed by injecting 5 μL of the sample onto a Phenomenex Luna C18 (2 × 50 mm, 3 μm) column. The flow conditions were 50% solvent A (water containing 0.1% formic acid) and 50% solvent B (acetonitrile containing 0.1% formic acid). The flow rate was 0.3 mL/min.

Statistics. For the CNV animal model, the experimental results obtained in the experiment were expressed as means ± SD and were tested using GraphPad Prism. The Shapiro−Wilk normality test was performed for all the data. When the normal distribution was followed, one-way analysis of variance (ANOVA) was performed. Additionally, Tukey's multiple comparison test was performed to determine the test group with a significant difference from the control group (excipient group). If not, the Kruskal−Wallis test was performed, and a post hoc test was performed with Dunn's multiple comparisons test (significance level: 5 and 1% on both sides). For the OIR animal model, data were presented as the mean ± SEM, and statistical significance was calculated using unpaired Student's *t*-test. All the other data were presented as means ± SD for at least two independently performed experiments. Statistical significance was determined by ANOVA using Dunnett's test (two-sided).

■ ASSOCIATED CONTENT

Supporting Information

The Supporting Information is available free of charge at https://pubs.acs.org/doi/10.1021/acs.jmedchem.0c01965.

> Selective index of all the final target compounds, IC_{50} graphs for tube formation and cell viability of **31**, VEGFR-2 kinase activity of **31**, DiscoverX KINOMEscan profiling of **31**, experimental procedures and spectroscopic data for all new compounds, and HRMS and HPLC analysis of the biologically tested compounds (PDF)
>
> Molecular formula strings (CSV)
>
> DiscoverX KINOMEscan profiling of **31** (CSV)

■ AUTHOR INFORMATION

Corresponding Authors

Sang Kook Lee − *College of Pharmacy, Seoul National University, Seoul 08826, Korea;* orcid.org/0000-0002-4306-7024; Phone: +82-2-880-2475; Email: sklee61@snu.ac.kr

Sanghee Kim − *College of Pharmacy, Seoul National University, Seoul 08826, Korea;* orcid.org/0000-0001-9125-9541; Phone: +82-2-880-2487; Email: pennkim@snu.ac.kr

Authors

Donghwa Kim − *College of Pharmacy, Seoul National University, Seoul 08826, Korea;* orcid.org/0000-0003-1425-213X

Sang Won Choi − *College of Pharmacy, Seoul National University, Seoul 08826, Korea*

Jihee Cho − *College of Pharmacy, Seoul National University, Seoul 08826, Korea;* orcid.org/0000-0002-1814-7794

Jae-Hui Been − *College of Pharmacy, Seoul National University, Seoul 08826, Korea*

Kyoungsun Choi − *College of Pharmacy, Seoul National University, Seoul 08826, Korea*

Wenzhe Jiang − *College of Pharmacy, Seoul National University, Seoul 08826, Korea*

Jaeho Han − *College of Pharmacy, Seoul National University, Seoul 08826, Korea*

Jedo Oh − *Hana Pharmaceutical Co., Pangyo 13486, Korea*

Changmin Park − *Hana Pharmaceutical Co., Pangyo 13486, Korea*

Soongyu Choi − *Hana Pharmaceutical Co., Pangyo 13486, Korea*

Songyi Seo − *Department of Global Innovative Drug, Graduate School of Chung-Ang University, College of Pharmacy, Chung-Ang University, Seoul 06974, Korea*

Koung Li Kim − *Department of Global Innovative Drug, Graduate School of Chung-Ang University, College of Pharmacy, Chung-Ang University, Seoul 06974, Korea*

Wonhee Suh − *Department of Global Innovative Drug, Graduate School of Chung-Ang University, College of Pharmacy, Chung-Ang University, Seoul 06974, Korea;* orcid.org/0000-0001-5811-0833

Complete contact information is available at: https://pubs.acs.org/10.1021/acs.jmedchem.0c01965

Author Contributions

D.K. and S.W.C. contributed equally to this work. All the authors have approved the final version of the manuscript.

Notes

The authors declare no competing financial interest.

■ ACKNOWLEDGMENTS

This work was supported by a grant from the Korea Health Technology R&D Project through the Korea Health Industry Development Institute (KHIDI), funded by the Ministry of Health & Welfare, Republic of Korea (grant number: HI18C1371).

■ ABBREVIATIONS

AMD, age-related macular degeneration; ANGPT2, angiopoietin-2; ARPE-19, adult retinal pigment epithelial cell line-19; CNV, choroidal neovascularization; CTF, corrected total fluorescence; DME, diabetic macular edema; DMEM/F-12, Dulbecco's modified Eagle's medium/nutrient mixture F-12; EBM, endothelial basal medium; EGM-2, endothelial cell growth medium-2; ERG, electroretinogram; EtOAc, ethyl acetate; EtOH, ethanol; FBS, fetal bovine serum; FES, tyrosine-protein kinase Fes/Fps; FTIR, Fourier-transform infrared; FYN, tyrosine-protein kinase Fyn; HRMECs, human retinal microvascular endothelial cells; HRP, horseradish peroxidase; HUVECs, human umbilical vein endothelial cells; IL-1β, interleukin 1 beta; MeCN, acetonitrile; MeOH, methanol; MTT, 3-(4,5-dimethylthiazol-2-yl)-2,5-diphenyltetrazolium bromide; OIR, oxygen-induced retinopathy; DR, proliferative diabetic retinopathy; PI3KCA, phosphatidylinositol-4,5-bisphosphate 3-kinase catalytic subunit alpha; PI3KR1, phosphatidylinositol 3-kinase regulatory subunit alpha; PVDF, polyvinylidene difluoride; ROP, retinopathy of prematurity; STAT5A, signal transducer and activator of transcription 5A; STAT5B, signal transducer and activator of transcription 5B; *t*-BuOH, *tert*-butyl alcohol; TBST, tris-buffered saline containing

0.1% Tween-20; TEK, TEK receptor tyrosine kinase; TGFβ1, transforming growth factor beta 1; Tie2, tunica interna endothelial cell kinase 2; TIMPs, tissue inhibitors of metalloproteinases

■ REFERENCES

(1) Fallah, A.; Sadeghinia, A.; Kahroba, H.; Samadi, A.; Heidari, H. R.; Bradaran, B.; Zeinali, S.; Molavi, O. Therapeutic Targeting of Angiogenesis Molecular Pathways in Angiogenesis-Dependent Diseases. *Biomed. Pharmacother.* **2019**, *110*, 775−785.

(2) Breier, G. Angiogenesis in Embryonic Development-A Review. *Placenta* **2000**, *21*, S11−S15.

(3) Felmeden, D.; Blann, A. D.; Lip, G. Y. H. Angiogenesis: Basic Pathophysiology and Implications for Disease. *Eur. Heart J.* **2003**, *24*, 586−603.

(4) Toomey, D. P.; Murphy, J. F.; Conlon, K. C. COX-2, VEGF and Tumor Angiogenesis. *Surgeon* **2009**, *7*, 174−180.

(5) Loukovaara, S.; Robciuc, A.; Holopainen, J. M.; Lehti, K.; Pessi, T.; Liinamaa, J.; Kukkonen, K.-T.; Jauhiainen, M.; Koli, K.; Keski-Oja, J.; Immonen, I. Ang-2 Upregulation Correlates with Increased Levels of MMP-9, VEGF, EPI, and TGFβ1 in Diabetic Eyes Undergoing Vitrectomy. *Acta Ophthalmol.* **2013**, *91*, 531−539.

(6) Duh, E. J.; Sun, J. K.; Stitt, A. W. Diabetic Retinopathy: Current Understanding, Mechanisms, and Treatment Strategies. *JCI insight* **2017**, *2*, No. e93751.

(7) Yau, J. W. Y.; Rogers, S. L.; Kawasaki, R.; Lamoureux, E. L.; Kowalski, J. W.; Bek, T.; Chen, S.-J.; Dekker, J. M.; Fletcher, A.; Grauslund, J.; Haffner, S.; Hamman, R. F.; Ikram, M. K.; Kayama, T.; Klein, B. E. K.; Klein, R.; Krishnaiah, S.; Mayurasakorn, K.; O'Hare, J. P.; Orchard, T. J.; Porta, M.; Rema, M.; Roy, M. S.; Sharma, T.; Shaw, J.; Taylor, H.; Tielsch, J. M.; Varma, R.; Wang, J. J.; Wang, N.; West, S.; Xu, L.; Yasuda, M.; Zhang, X.; Mitchell, P.; Wong, T. Y. Global Prevalence and Major Risk Factors of Diabetic Retinopathy. *Diabetes Care* **2012**, *35*, 556−564.

(8) Tarr, J. M.; Kaul, K.; Wolanska, K.; Kohner, E. M.; Chibber, R. Retinopathy in Diabetes. *Adv. Exp. Med. Biol.* **2012**, *771*, 88−106.

(9) Harris Nwanyanwu, K.; Talwar, N.; Gardner, T. W.; Wrobel, J. S.; Herman, W. H.; Stein, J. D. Predicting Development of Proliferative Diabetic Retinopathy. *Diabetes Care* **2013**, *36*, 1562−1568.

(10) Bressler, S. B.; Liu, D.; Glassman, A. R.; Blodi, B. A.; Castellarin, A. A.; Jampol, L. M.; Kaufman, P. L.; Melia, M.; Singh, H.; Wells, J. A. Change in Diabetic Retinopathy Through 2 Years: Secondary Analysis of a Randomized Clinical Trial Comparing Aflibercept, Bevacizumab, And Ranibizumab. *JAMA Ophthalmol.* **2017**, *135*, 558−568.

(11) Yu, S.; Oh, J.; Li, F.; Kwon, Y.; Cho, H.; Shin, J.; Lee, S. K.; Kim, S. New Scaffold for Angiogenesis Inhibitors Discovered by Targeted Chemical Transformations of Wondonin Natural Products. *ACS Med. Chem. Lett.* **2017**, *8*, 1066−1071.

(12) Cifuentes, T.; Cayupi, J.; Celis-Barros, C.; Zapata-Torres, G.; Ballesteros, R.; Ballesteros-Garrido, R.; Abarca, B.; Jullian, C. Spectroscopic Studies of the Interaction of 3-(2-Thienyl)-[1,2,3]-Triazolo[1,5-*a*] Pyridine with 2,6-Dimethyl-β-Cyclodextrin and *ct*DNA. *Org. Biomol. Chem.* **2016**, *14*, 9760−9767.

(13) Hirose, W.; Sato, K.; Matsuda, A. Fluorescence Properties of 5-(5,6-Dimethoxybenzothiazol-2-yl)-2′-deoxyuridine ($\mathrm{d^{bt}U}$) and Oligodeoxyribonucleotides Containing $\mathrm{d^{bt}U}$. *Eur. J. Org. Chem.* **2011**, *2011*, 6206−6217.

(14) Pfaendler, H. R.; Weimar, V. Synthesis of Racemic Ethanolamine Plasmalogen. *Synthesis* **1996**, *1996*, 1345−1349.

(15) Abhinand, C. S.; Raju, R.; Soumya, S. J.; Arya, P. S.; Sudhakaran, P. R. VEGF-A/VEGFR2 Signaling Network in Endothelial Cells Relevant to Angiogenesis. *J. Cell Comm. Signal.* **2016**, *10*, 347−354.

(16) Lamalice, L.; Le Boeuf, F.; Huot, J. Endothelial Cell Migration during Angiogenesis. *Circ. Res.* **2007**, *100*, 782−794.

(17) Patel, J. I.; Hykin, P. G.; Gregor, Z. J.; Boulton, M.; Cree, I. A. Angiopoietin Concentrations in Diabetic Retinopathy. *Br. J. Ophthalmol.* **2005**, *89*, 480−483.

(18) Hammes, H.-P.; Lin, J.; Wagner, P.; Feng, Y.; vom Hagen, F.; Krzizok, T.; Renner, O.; Breier, G.; Brownlee, M.; Deutsch, U. Angiopoietin-2 Causes Pericyte Dropout in the Normal Retina: Evidence for Involvement in Diabetic Retinopathy. *Diabetes* **2004**, *53*, 1104−1110.

(19) Takagi, H.; Koyama, S.; Seike, H.; Oh, H.; Otani, A.; Matsumura, M.; Honda, Y. Potential Role of the Angiopoietin/Tie2 System in Ischemia-Induced Retinal Neovascularization. *Invest. Ophthalmol. Visual Sci.* **2003**, *44*, 393−402.

(20) Peters, S.; Cree, I. A.; Alexander, R.; Turowski, P.; Ockrim, Z.; Patel, J.; Boyd, S. R.; Joussen, A. M.; Ziemssen, F.; Hykin, P. G.; Moss, S. E. Angiopoietin Modulation of Vascular Endothelial Growth Factor: Effects on Retinal Endothelial Cell Permeability. *Cytokine* **2007**, *40*, 144−150.

(21) Hussain, R. M.; Neiweem, A. E.; Kansara, V.; Harris, A.; Ciulla, T. A. Tie-2/Angiopoietin Pathway Modulation as a Therapeutic Strategy for Retinal Disease. *Expert Opin. Invest. Drugs* **2019**, *28*, 861−869.

(22) Cheng, K.-J.; Hsieh, C.-M.; Nepali, K.; Liou, J.-P. Ocular Disease Therapeutics: Design and Delivery of Drugs for Diseases of the Eye. *J. Med. Chem.* **2020**, *63*, 10533−10593.

(23) Papadopoulos, K. P.; Kelley, R. K.; Tolcher, A. W.; Razak, A. R. A.; Van Loon, K.; Patnaik, A.; Bedard, P. L.; Alfaro, A. A.; Beeram, M.; Adriaens, L.; Brownstein, C. M.; Lowy, I.; Kostic, A.; Trail, P. A.; Gao, B.; DiCioccio, A. T.; Siu, L. L. A Phase I First-in-Human Study of Nesvacumab (REGN910), a Fully Human Anti-Angiopoietin-2 (Ang2) Monoclonal Antibody, in Patients with Advanced Solid Tumors. *Clin. Cancer Res.* **2016**, *22*, 1348−1355.

(24) Schneider, H.; Szabo, E.; Machado, R. A. C.; Broggini-Tenzer, A.; Walter, A.; Lobell, M.; Heldmann, D.; Süssmeier, F.; Grünewald, S.; Weller, M. Novel TIE-2 Inhibitor BAY-826 Displays *in vivo* Efficacy in Experimental Syngeneic Murine Glioma Models. *J. Neurochem.* **2017**, *140*, 170−182.

(25) Harney, A. S.; Karagiannis, G. S.; Pignatelli, J.; Smith, B. D.; Kadioglu, E.; Wise, S. C.; Hood, M. M.; Kaufman, M. D.; Leary, C. B.; Lu, W.-P.; Al-Ani, G.; Chen, X.; Entenberg, D.; Oktay, M. H.; Wang, Y.; Chun, L.; De Palma, M.; Jones, J. G.; Flynn, D. L.; Condeelis, J. S. The Selective Tie2 Inhibitor Rebastinib Blocks Recruitment and Function of $\mathrm{Tie2^{Hi}}$ Macrophages in Breast Cancer and Pancreatic Neuroendocrine Tumors. *Mol. Cancer Ther.* **2017**, *16*, 2486−2501.

(26) Sahni, J.; Patel, S. S.; Dugel, P. U.; Khanani, A. M.; Jhaveri, C. D.; Wykoff, C. C.; Hershberger, V. S.; Pauly-Evers, M.; Sadikhov, S.; Szczesny, P.; Schwab, D.; Nogoceke, E.; Osborne, A.; Weikert, R.; Fauser, S. Simultaneous Inhibition of Angiopoietin-2 and Vascular Endothelial Growth Factor-A with Faricimab in Diabetic Macular Edema: BOULEVARD Phase 2 Randomized Trial. *Ophthalmology* **2019**, *126*, 1155−1170.

(27) Szklarczyk, D.; Gable, A. L.; Lyon, D.; Junge, A.; Wyder, S.; Huerta-Cepas, J.; Simonovic, M.; Doncheva, N. T.; Morris, J. H.; Bork, P.; Jensen, L. J.; Mering, C. V. STRING V11: Protein-Protein Association Networks with Increased Coverage, Supporting Functional Discovery in Genome-Wide Experimental Datasets. *Nucleic Acids Res.* **2019**, *47*, D607−D613.

(28) Yang, X.; Qiao, D.; Meyer, K.; Friedl, A. Signal Transducers and Activators of Transcription Mediate Fibroblast Growth Factor-Induced Vascular Endothelial Morphogenesis. *Cancer Res.* **2009**, *69*, 1668−1677.

(29) Yang, X.; Meyer, K.; Friedl, A. STAT5 and Prolactin Participate in a Positive Autocrine Feedback Loop That Promotes Angiogenesis. *J. Biol. Chem.* **2013**, *288*, 21184−21196.

(30) Kim, H. W.; Kim, J. L.; Lee, H. K.; Hur, D. Y.; Yun, I. H.; Kim, S. D. Enalapril Alters Expression of Key Growth Factors in Experimental Diabetic Retinopathy. *Curr. Eye Res.* **2009**, *34*, 976−987.

(31) Lee, M. Y.; Gamez-Mendez, A.; Zhang, J.; Zhuang, Z.; Vinyard, D. J.; Kraehling, J.; Velazquez, H.; Brudvig, G. W.; Kyriakides, T. R.;

Simons, M.; Sessa, W. C. Endothelial Cell Autonomous Role of Akt1. *Arterioscler., Thromb., Vasc. Biol.* **2018**, *38*, 870−879.

(32) Graupera, M.; Guillermet-Guibert, J.; Foukas, L. C.; Phng, L.-K.; Cain, R. J.; Salpekar, A.; Pearce, W.; Meek, S.; Millan, J.; Cutillas, P. R.; Smith, A. J. H.; Ridley, A. J.; Ruhrberg, C.; Gerhardt, H.; Vanhaesebroeck, B. Angiogenesis Selectively Requires the P110α Isoform of PI3K to Control Endothelial Cell Migration. *Nature* **2008**, *453*, 662−666.

(33) Gesbert, F.; Griffin, J. D. Bcr/Abl Activates Transcription of the Bcl-X Gene through STAT5. *Blood* **2000**, *96*, 2269−2276.

(34) Kharas, M. G.; Fruman, D. A. ABL Oncogenes and Phosphoinositide 3-Kinase: Mechanism of Activation and Downstream Effectors. *Cancer Res.* **2005**, *65*, 2047−2053.

(35) Murugeswari, P.; Shukla, D.; Rajendran, A.; Kim, R.; Namperumalsamy, P.; Muthukkaruppan, V. Proinflammatory Cytokines and Angiogenic and Anti-Angiogenic Factors in Vitreous of Patients with Proliferative Diabetic Retinopathy and Eales′ Disease. *Retina* **2008**, *28*, 817−824.

(36) Petrovič, MG; Korošec, P.; Košnik, M.; Hawlina, M. Association of Preoperative Vitreous IL-8 and VEGF Levels with Visual Acuity after Vitrectomy in Proliferative Diabetic Retinopathy. *Acta Ophthalmol.* **2010**, *88*, e311−6.

(37) Capitão, M.; Soares, R. Angiogenesis and Inflammation Crosstalk in Diabetic Retinopathy. *J. Cell. Biochem.* **2016**, *117*, 2443−2453.

(38) Avdeef, A. pH-metric Solubility. 1. Solubility-pH Profiles from Bjerrum Plots. Gibbs Buffer and pKa in the Solid State. *Pharm. Pharmacol. Commun.* **1998**, *4*, 165−178.

(39) Etherson, K.; Halbert, G.; Elliott, M. Determination of Excipient Based Solubility Increases using the CheqSol Method. *Int. J. Pharm.* **2014**, *465*, 202−209.

(40) Fabian, M. A.; Biggs, W. H., 3rd; Treiber, D. K.; Atteridge, C. E.; Azimioara, M. D.; Benedetti, M. G.; Carter, T. A.; Ciceri, P.; Edeen, P. T.; Floyd, M.; Ford, J. M.; Galvin, M.; Gerlach, J. L.; Grotzfeld, R. M.; Herrgard, S.; Insko, D. E.; Insko, M. A.; Lai, A. G.; Lélias, J.-M.; Mehta, S. A.; Milanov, Z. V.; Velasco, A. M.; Wodicka, L. M.; Patel, H. K.; Zarrinkar, P. P.; Lockhart, D. J. A Small Molecule-Kinase Interaction Map for Clinical Kinase Inhibitors. *Nat. Biotechnol.* **2005**, *23*, 329−336.